DNS of heat transfer in a turbulent channel flow over fractal roughness

Pranav Suvarna

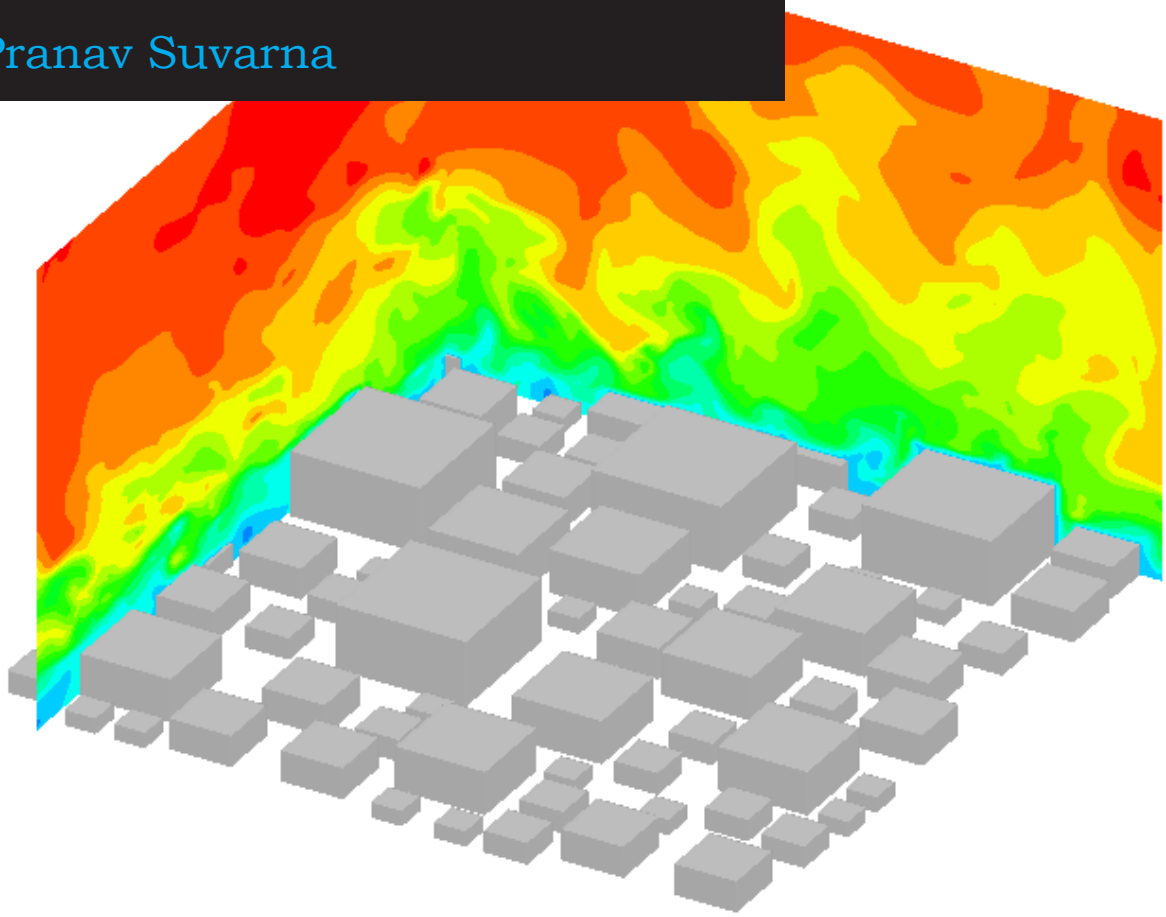

Technische Universiteit Delft

TU Delft Delft University of Technology

Challenge the future

DNS of heat transfer in a turbulent channel flow over fractal roughness

by

Pranav Suvarna

in partial fulfillment of the requirements for the degree of

Master of Science

in Mechanical Engineering

at the Delft University of Technology,

to be defended publicly on Wednesday August 12, 2020 at 11:00 AM.

P&E Report Number: 3027

Supervisors:	Prof. dr. ir. W. van de Water,	TU Delft
	Dr. ir. M.J.B.M. Pourquie,	TU Delft
Thesis committee:	Dr ir. J.W.R. Peeters,	TU Delft
	Dr. A. Laskari,	TU Delft

TU Delft Delft University of Technology

Acknowledgements

I would like to thank my supervisors Prof.dr.ir. Willem van de Water and Dr.ir.Mathieu Pourquie for their technical supervision and guidance on my thesis and also for extending moral support during my tough phases. Furthermore, I would like to thank Dr.ir.Jurriaan Peeters and Dr. Angeliki Laskari for accepting to be part of the thesis committee.

I would further like to extend my gratitude towards my academic counsellor Evert Vixseboxse who has been constantly supporting me during the difficult phase of my thesis.

Special thanks goes out to my friends Prasad, Naveen, Vinayak, Saurabh, Kyana and Sreekar who have made this journey fun and memorable. Also, I would like to thank my parents, uncle and my sisters Nidhi and Raksha for their love, support and encouragement.

Finally, I would like to thank TU Delft and the department of Fluid Mechanics for giving me an opportunity to study here and for providing a dynamic learning environment.

Pranav Suvarna
Delft, August 2020

Abstract

Convective heat transfer finds applications in several domains of industry like heat exchangers, gas turbine blades, IC engine surfaces etc. The surfaces of these heat transfer applications are either naturally rough owing to manufacturing techniques or become rough over a period of time during operation. These rough surfaces usually contain multiple length scales and exhibit random and heterogenous properties. Fractal roughness, in principal, is characterized by self-similar detail on smaller and smaller length scales and hence fractal dimension which is independent of any length scale can become a very viable option to characterize these multi-scale random surfaces. Therefore in the current thesis, rough surfaces characterized by fractal dimensions were designed and their role in the heat transfer enhancement relative to the pressure drop was studied using DNS.

The fractal surfaces were designed by randomly placing five generations of self-similar cuboids with decreasing sizes from higher to lower generations. The quantity of cuboids sprinkled randomly for each generation followed a fractal dimension. Two principal fractal dimensions were selected, i.e $D = 1$ and $D = 2$ and eight random realizations of each were generated in order to study the averaged effect of the heat transfer performance. Since the cuboids were randomly placed, different realizations within the same fractal dimension experienced varied sheltering effects by larger generation cuboids. This ultimately produced a fluctuation in the ”sheltered” solidity of the fractal surface for different realizations whose effect was also studied. The cuboids were resolved in the simulation using an immersed boundary method [1].

To quantify the heat transfer performance of the rough surfaces, two performance factors namely the aero-thermal efficiency (η_a) and Reynolds analogy factor (RA/RA_0) were defined. It was found that the two types of fractal surfaces performed approximately similarly with a slight higher mean for $D = 2$ based on the above heat performance parameters even though the two surfaces looked very different. However, the above performance factors showed a very strong correlation with the ”sheltered” solidity of the fluctuating realizations displaying an increasing trend.

Contents

List of Tables

List of Figures

1

Introduction

1.1. Turbulent flows

It is very easy to observe examples of turbulent flows in our daily surroundings. Be it the smoke emanating from a chimney or a jet engine, air flows around vehicles or atmospheric flows around buildings. Despite being such a wide spread and common phenomenon, turbulence still remains one of the most difficult phenomena to define in physics. On first glance, these flows may seem to look very random and chaotic, however when studied closely we observe certain distinct patterns and characteristics. One such characteristic is that these flows contain numerous eddies with different sizes that constantly interact with each other. These eddies have a significant impact on the fluid flow and they help us to understand the distribution of various features such as pressure, velocity and temperature etc. which can be useful in modelling various engineering flow applications. Another important property of a turbulent flow is that it is diffusive i.e it is very effective in mixing fluids. This property is certainly a boon in many applications, ranging from simplistic cases like efficient mixing of our morning coffee to efficient dissipation of heat required in cooling applications. This property of turbulence was demonstrated by Osborne Reynolds in his famous experiment in 1883 as shown in figure 1.1. As it can be seen, the flow is not always turbulent i.e. it can also be laminar (more ordered) and it's transition to turbulence is governed by a quantity that is defined as the Reynolds Number. Turbulence usually occurs at higher values of Reynolds number.

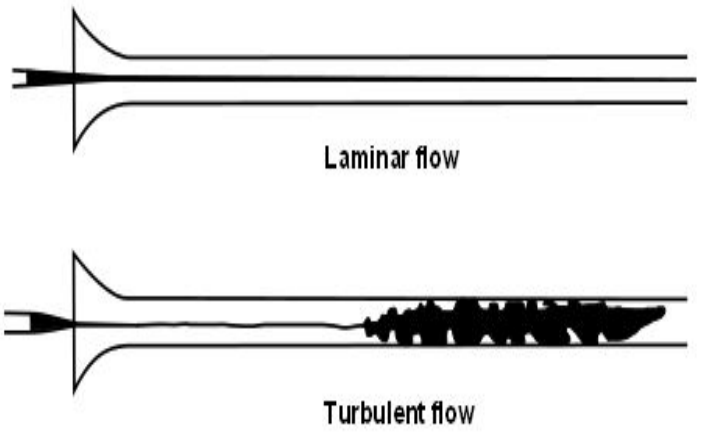

Figure 1.1: Onset of turbulent flows depicted by mixing of dye from an experiment conducted by Reynolds [2]

In addition to the Reynolds number criterion, the transition to turbulence can also be triggered by

inserting certain passive disturbances on walls which is obtained by modifying the shape and surface of the walls. This is widely used in the sports cycle/car racing industry where the earlier transition to turbulence is sometimes favoured so as to make use of the mixing property of turbulence. Small disturbances are added on the helmets of cyclists or towards the rear of racing cars (vortex generators) to enforce turbulence which delays the separation of the low energy laminar boundary layer by mixing the high momentum fluid in the outer field with the low momentum fluid within the boundary layer thereby reducing drag. Besides artificially adding these disturbances, natural surfaces (in most engineering applications) tend to be very rough with varied size and shape distributions in different directions. On account of this, it is important to understand the interaction of the flow with these multi-scale rough walls so that they can be modelled.

The mixing property of turbulence, specifically for applications where heat transfer is involved will be explored in this thesis in particular on rough wall surfaces. This will be described further in the next subsection.

1.2. Convective Heat transfer

Convection is one of the three modes of heat transfer which is governed by the bulk motion of fluid as compared to conduction which occurs due to molecular motion and radiation which occurs through electromagnetic waves. Convective heat transfer occurs whenever a fluid flows over a hot/cold surface and it finds applications in numerous industrial processes and heating/cooling devices. It is usually expressed in terms of a heat transfer co-efficient (h) defined as:

$$h = \frac{Q_{conv}}{A_{surf}(T_{surf} - T_{bulk})} \tag{1.1}$$

where Q_{conv} is the convective heat transferred from the surface to the fluid, A_{surf} refers to the surface area and T_{surf} & T_{bulk} refers to the averaged surface temperature and the bulk fluid temperature whose difference drives the heat exchange. In order to gain a better insight into the physics and quantify the effectiveness of heat transfer due to fluid flow over a surface, it is convenient to non-dimensionalize the heat transfer co-efficient with relevant parameters. Two such parameters which are often used are the Nusselt number, $Nu = hL/\lambda$ (where, L is the characteristic length scale and λ is the thermal conductivity of the fluid) and the Stanton number, $St = h/\rho C_p U_{bulk}$ (where ρ is the fluid density, C_p is the specific heat capacity & U_{bulk} is the fluid bulk velocity). For simple geometries like pipe/channel flow, the convective heat transfer is directly related to air flow and therefore, the Nusselt number can be expressed in terms of Reynolds number and Prandtl number [3]:

$$Nu = ARe_L^m Pr^n f(inbox(geometry)) \tag{1.2}$$

where Pr is the Prandtl number, ($Pr = \nu/\alpha$, where ν & α are the viscosity and thermal diffusivity of the fluid respectively), A is a constant, n and m are correlation coefficients and $f(inbox(geometry))$ is a function dependent on geometry.

Similarly for simple geometries, Reynolds suggested that the heat and momentum transfer are caused by the same physical mechanism which is expressed by the classical relation as given below [3]:

$$St_x = \frac{1}{2} C_{f,x} \tag{1.3}$$

where St_x is the local Stanton number, based on the local heat transfer coefficient, and $C_{f,x}$ is the local friction factor, defined as $C_{f,x} = 2\tau_w/\rho U_{bulk}^2$ where τ_w is the wall shear stress. From this, a relation between the local heat transfer and fluid flow near the wall can be deduced as below [3]:

$$h \sim \frac{\tau_w}{U_{bulk}} \tag{1.4}$$

But the relations mentioned in eqn. 1.2 & 1.4 estimate the convective heat transfer with correct order of magnitude only for simple geometries with single characteristic length scales like pipe/channel

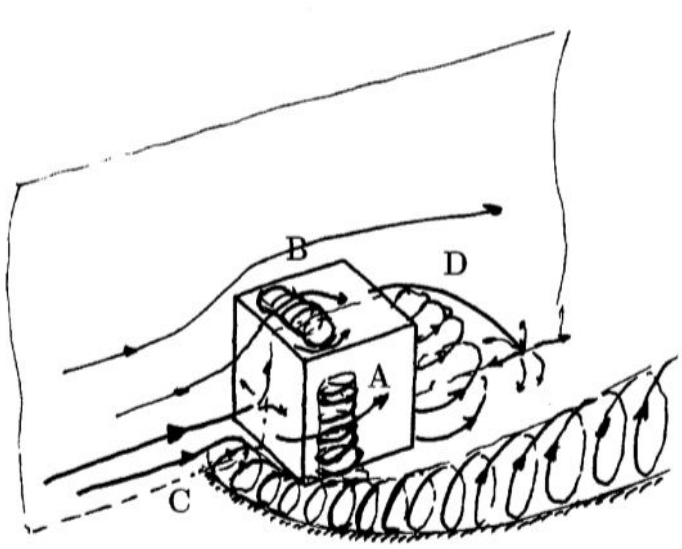

Figure 1.2: Flow features around single cube in turbulent channel flow as represented by an artist. A-side vortex, B-top vortex, C-horseshoe vortex & D-wake vortex. [3]

flow with smooth walls. Nevertheless, realistic surfaces for practical engineering applications tend to be very complex, rough, spatially heterogeneous and irregular in nature (for example, rough pipes/turbine blades that are affected by operational issues like erosion, deposition & spallation etc. [7] or flows over wall mounted cubes for cooling applications) and consist of multiple length scales. These multi-scale roughness elements ultimately interfere with the dynamics of the flow & heat transfer near the wall which causes deviations from these correlations [3]. Three dimensional roughness elements act as bluff bodies and significantly affect the flow structure near the wall by producing separations, re-circulations and reattachment zones. Figure 1.2 shows the complex three dimensional nature of flow around a single cube that is governed by different vortical structures like the horseshoe vortex (C), wake vortex (D) and top (B) & side (A) vortices which would be absent in smooth wall cases. In this work this is a very relevant case, as we will construct roughness using a collection of surface mounted cubes.

These vortical structures can lead to steep spatial gradients in the distribution of the convective heat transfer [3]. In addition to the above, periodic flow phenomena like vortex shedding can also emerge due to flow instabilities arising from separation at sharp edges and these can affect the time dependent convective heat transfer in the roughness layer [3]. The interaction between vortical structures can differ between different topologies of rough surfaces which ultimately affects the convective heat transfer and hence further research needs to be done for these complex surfaces. In the next section we review some of the relevant literature for flow and heat transfer over complex surfaces.

1.3. Literature review: Turbulent flow over rough surfaces & scalar dispersion

From the previous section, we learnt that smooth wall correlations (eqn. 1.2 & 1.4) cannot be directly applied to rough wall geometries due to various complexities induced in the flow. We therefore, do a comprehensive literature search in order to study the flow dynamics occurring due to these roughness elements which cause the departure from smooth wall correlations. It is essential to note that the driving potential for heat $(T_w - T_\infty)$ and mass $(\rho_w - \rho_\infty)$ transfer in dilute solutions are equivalent when the transport of a passive scalar is considered between wall and free stream [8]. Therefore, analogous studies for mass transfer over complex surfaces are also highlighted in the literature below.

As briefly mentioned earlier, the surface quality for practical engineering applications tends to be very

rough, spatially heterogeneous and highly irregular in nature. For example, the surfaces of turbine blades & heat exchanger pipes tend to become very rough during their life cycle due to various reasons like erosion, deposition & spallation etc. that affect the convective heat transfer and skin friction as compared to their smooth wall counterparts [7]. In addition to life cycle operational reasons, many applications that involve the use of novel additive manufacturing techniques for IC engine surfaces can make them very rough as well [7]. Besides applications in practical engineering problems, realistic ground surfaces for atmospheric flows over urban or rural terrains (buildings, trees & mountains etc.) are also very rough with elements displaying a range of shape complexities and size distributions [4]. Before diving into the literature for rough wall flows, let us briefly talk about the important regions for turbulent flows over smooth walls and then discuss the impact of roughness elements on these regions.

Classical textbooks like Pope [9] & Nieuwstadt *et al.* [10] have given a detailed explanation of the structure of smooth wall bounded turbulent flows. Generally, smooth wall bounded flows are governed by two sets of scales, namely, one very close to the wall called the inner layer and the other very far from the wall called the outer layer. For the inner layer, viscosity plays an important role and the relevant scaling parameters are friction velocity ($u_\tau = \sqrt{\tau_w/\rho}$, where τ_w and ρ are the wall shear stress and fluid density respectively) and the viscous wall unit (δ_v, where $\delta_v = \nu/u_\tau$). Within this inner layer, there is a region called the viscous sub-layer which is very close to the wall and the buffer layer which is a little further away from the wall and it is responsible for generating most of the turbulent energy. On the other hand for the outer layer, the size of the turbulent structures are limited by the boundary layer thickness (δ) which becomes the relevant length scale [11]. For fully developed turbulent flows, there is also a layer between the outer and buffer region where the relevant length scale is it's distance from the wall and which follows a logarithmic profile for the stream wise velocity. This layer is called the logarithmic layer and is also responsible for contributing majorly to the overall production of turbulent energy [11].

However when roughness elements are present on the surface, depending on their height they can interfere with the scales of smooth wall flows described above. If the height (k) of roughness exceeds a few wall units, they interfere with the operation of the buffer-layer and completely destroy it when $k^+ \geq 5{-}100$ (where, $k^+ = k/\delta_v$) [11]. For the case of rough wall flows, the viscous sublayer for 'smooth wall' flows is replaced by the roughness sub-layer [12] the dynamics of which is important to understand in order to model the flow or dispersion processes in urban environments or rough channels. Within the roughness sublayer, the mean flow exhibits spatial variability associated with geometric attributes of topographic elements, while above this (in the inertial layer) the mean flow (stream wise velocity component) tends to a logarithmic profile and the turbulence structural attributes are unaffected by the topography [12]. In the next section, we present some of the parameters most commonly used in turbulent flow studies for characterizing rough surfaces.

1.3.1. Roughness Parameters

An important reason for implementing various roughness parameters for defining rough surfaces is to simplistically model their complex nature in terms of a momentum deficit (increased drag) that they add to their smooth wall flow counterpart [12]. However, our aim is not to make any model for the rough surface but to study the flow dynamics that occur in the roughness sub layer by manipulating the surface heterogeneity of the wall. A comprehensive guide on the different roughness parameters used both for engineering applications and atmospheric flows with relevant roughness models for predicting the drag reduction are given in Flack and Schultz [13], Grimmond and Oke [14] & Zhu *et al.* [12]. In this section, we simply highlight some of the important parameters that can be used to define our surfaces' heterogeneity.

For engineering applications, an important parameter that represents the effect of the roughness is the equivalent sand roughness height k_s which was first defined by Schlichting [15] from the sizes of the sand grains in Nikuradse's experiments [16] that produce the same friction coefficient as the rough surface [13]. However, k_s is a representative roughness scale that only models the bulk effect of the wall on the momentum deficit but does not really give us any insight of the flow structure/dynamics in the roughness sub layer [17]. Nevertheless, it remains an important parameter as it helps us in

distinguishing between hydraulically smooth ($k_s^+ < 5$), transitionally rough ($5 < k_s^+ \leq 70$), and fully rough ($k_s^+ \geq 70$) walls, with $k_s^+ = k_s/\delta_\nu$ [17].

An analogous counterpart of k_s in atmospheric flows is given by the aerodynamic roughness length z_0. It is used in conjunction with the zero-plane displacement d to model the cumulative effect of flow separation over an urban terrain (plant canopies, multiple sizes of buildings etc.) in terms of the mean momentum deficit (aerodynamic drag) [12]. In this case, z_0 is interpreted as the effective height at which $U = 0$ and d is the elevation at which the mean surface drag acts [12].

Even though, z_0 & k_s have constraints in intrinsically describing the roughness topography yet they can act as a common language to describe the bulk effect of different surfaces for modelling engineering and atmospheric surfaces [12] [13]. Therefore, there have been attempts to predict the values of z_0 & k_s for rough surfaces by using additional parameters describing the geometry in terms of spatial distribution, density of arrangement of elements and their shape. It is common to model z_0 using the surface areal density parameters like the frontal area density ($\lambda_f = A_f/A_d$) and plan area density ($\lambda_p = A_p/A_d$) [12] (where, A_f, A_d and A_p are the total frontal area of obstacles, total bottom surface area and total plan area covered by obstacles respectively). Another parameter that is used is Λ_s which was introduced by Van Rij *et al.* [18] who tested it for irregular, three dimensional roughness [13]. This parameter combines the effect of the density of roughness elements given by (A_d/A_f) and the shape factor for the roughness elements (A_f/A_s).

$$\Lambda_s = \frac{A_d}{A_f}\left(\frac{A_f}{A_s}\right)^{-1.6} \tag{1.5}$$

where A_s is the total windward wetted surface area.

For complex roughness, the above areal parameters still do no completely capture the spatial heterogeneity and therefore statistical relations are sometimes suited to describe the surface. Flack and Schultz [13] (for engineering flows) studied the effect of statistical parameters and concluded that the rms value of roughness height (k_{rms}) and skewness (s_k) had a strong influence on k_s while the kurtosis of the surface had a negligible impact which was also confirmed by Zhu *et al.* [12] (for heterogeneous buildings in atmospheric flows). The skewness, s_k characterizes the asymmetry of the distribution of local surface elevations k, $s_k =< (k - < k >)^3 >$. Surfaces that are roughnened over time by the accumulation of deposits (like exhaust particulates, fouling etc.) generally have positive skewness while those surfaces that are pitted (like by corrosion, surface wear etc.) have negative skewness [13]. In table 1.1 we summarize the different roughness parameters described above along with a few studies in which they were included.

Table 1.1: List of parameters used to characterize roughness elements

Roughness Parameter	**Symbol**	**Shapes**	**Reference**
Equivalent Sandgrain roughness	k_s	Sandgrains & other shapes [1]	[13]
Roughness Length & Displacement height	z_0, d	Cuboids	[14],[12],[4], [19],[6],[20]
Frontal Density & Plan Density	λ_f, λ_p	Cuboids	[14],[12],[4], [19],[6],[20],[7]
Combined Density & Shape Parameter	Λ_s	Pyramids & other shapes [1]	[13], [7]
Standard deviation & Skewness	k_{rms}, s_k	Cuboids & other shapes [1]	[13],[12]

We will be using some of the above mentioned parameters along with the fractal dimension of the surface to interpret the effect of a multi-scale surface described in Chapter 2 on the turbulent flow & heat transfer.

1.3.2. Studies on turbulent flows and scalar dispersion over rough surfaces with cubical geometry

Studies on flows over rough surfaces have focused on different shapes of roughness elements like sand grain roughness, pyramids, hemispheres, cubes, riblets etc. which can be quantified and modelled by the parameters mentioned in section 1.3.1. In this thesis though, we would like to focus only on cubical shaped elements but with a broad range of size distributions. As mentioned earlier in section 1.2, roughness elements interfere with the dynamics of smooth wall flows; hence it is vital to understand the flow dynamics and the corresponding scalar dispersion (heat transfer) over complex terrains which could later be used to model them. Differing shapes, sizes and distribution of roughness elements can have varying effects on mean vertical profiles, turbulence intensities and vertical fluxes. We again note here that the driving potential for mass & heat transfer are the same when modelled as a passive scalar and hence we also mention analogous studies for mass transfer here.

As described earlier in section 1.2, the flow separation, reattachment & impingement dictates the local heat transfer phenomena near simple 2-D square cross-section obstacles. Numerous studies have been done which substantiate the above statement with a lot of data available from experiments (Aliaga *et al.* [21]) and DNS (Orlandi *et al.* [22], Miyake *et al.* [23]) to name a few. Extending to a 3-D case, flows over arrays of cubes have been studied along with local convective heat transfer by Chyu and Natarajan [8] who studied heat transfer over 3D protruding elements, Anderson [24] & Meinders [3] who studied matrix of cubes and studied the heat transfer co-efficient variation which was again found to be dictated by 3D vortex structures in the vicinity of the cubes. Another important phenomenon that augments the turbulent heat transfer in the boundary layer is the periodic vortex shedding phenomenon as demonstrated in experiments performed by Wroblewski and Eibeck [25]. Analogous studies in the atmospheric flows domain have been conducted for arrays of cubes arranged in an ordered manner (either inline or staggered) (Tomas [6], Coceal *et al.* [26], Belcher [27] & Macdonald *et al.* [28]). The cubes used in the above studies however, were of the same size with uniform spacing between them in the domain but they all nonetheless established the strong influence of 3D vortex structures in the vicinity of the cubes.

But natural rough surfaces exhibit multiscale, random and heterogeneous properties as opposed to the single scale studies mentioned above. This was first explored by Cheng and Castro [20] who studied an array of cuboids with height variation following a normal distribution but having uniform spacing between cubes and compared them with single sized homogeneous cube arrangement. They again confirmed the highly 3D nature of the flow and also found that the height of the roughness sub-layer was thicker for the heterogeneous case (height variation) in comparison to the homogeneous one. As mentioned in section 1.3.1, using statistical moments sometimes gives a better description of the surface topography. This was recently explored by Zhu *et al.* [12] who conducted LES studies for flow over cuboids arranged in a random manner and varied the values of rms ($< (h - < h >)^2 >^{1/2}$) and skewness of the height distribution.

Another interesting aspect of natural surfaces as first noted by Mandelbrot [29] is that many of it's features demonstrate fractal properties, including the height distribution of eroded surfaces and the layout of urban sprawl. In various studies on experimentally mapping rough surfaces, it was found that their anatomy follows a fractal pattern wherein under repeated magnification of the surface similar images emerge [30]. Also, as established earlier rough surfaces have several length scales and hence it is sometimes easier to characterize it using parameters that are independent of any length scale and so using fractals to describe the same becomes a very viable option [30] [4]. Therefore, in this work we use fractals to describe rough surfaces (Chapter 2).

Recently, there has been a growing interest in studying flows over fractal surfaces (both in engineering and atmospheric applications). One interesting study was done by Chen *et al.* [31] who studied the heat transfer in micro-channels for laminar flow over fractal surfaces described by a Weirstrass-Mandelbrot function with varying fractal dimension (D). They found that the flow convective heat transfer performance was optimized with increasing fractal dimension of the surface. However, we would like to focus on cubical roughness elements to form the fractal surface. Yang and Meneveau [4] examined flow past multi-scale surfaces that consisted of randomly placed cuboids whose number quadrupled as

the size of their edges were halved. As will be explained in chapter 2, the fractal dimension of such a rough surface is two, so it is strictly not a fractal. The surface designed in this study is illustrated in figure 1.3 which also formed the inspiration for our current study. The rough surface designed in Chapter 2 will be using similar cuboids arranged in a random manner but now in a way such that the fractal dimension is varied. However, the study of (Yang and Meneveau [4]) was majorly focused on developing an analytical roughness model for multi-scale terrains in atmospheric flows and only few results for mean structure of the flow with respect to the surface were presented. Of late, another interesting study was done by Vanderwel and Ganapathisubramani [19] who created fractal surfaces with cubical base structures akin to an ordered Sierpienski carpet with a similar power law height distribution (like Yang and Meneveau [4]) but they randomized the positioning of the cuboids. They varied the frontal density (λ_f) and the packing density (spacing between cubes) for different random fractal surfaces to study their effect on turbulent stresses & mean flow velocities and also compared them with the ordered Sierpienski carpet.

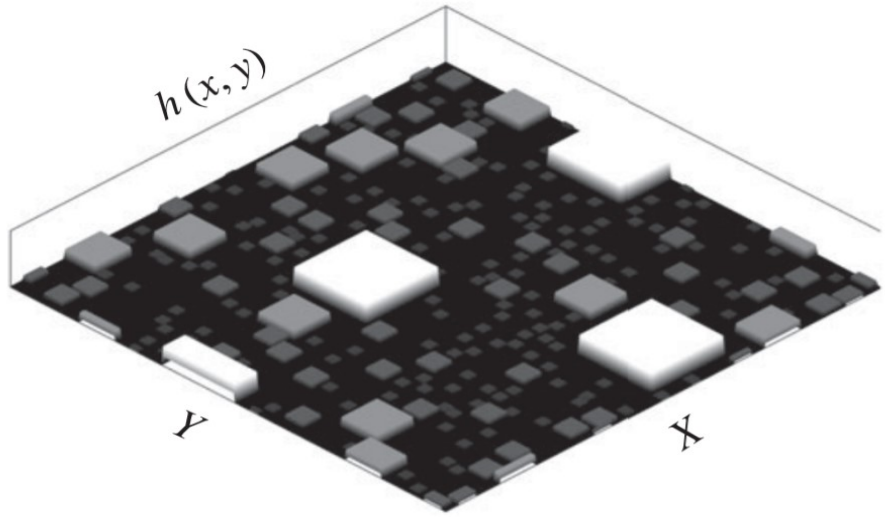

Figure 1.3: Rough wall synthesized using self-similar rectangular roughness elements. Reproduced from Yang and Meneveau [4]

Nonetheless, in the above studies the fractal dimension of the cubical structure has not been varied and it's relation with the hydrodynamic performance has not been established. Moreover, none of the above works have investigated the heat transfer over such surfaces which will be our scope of interest. Therefore in the current study, we intend to extend the works of Yang and Meneveau [4] and Vanderwel and Ganapathisubramani [19] to study the hydrodynamic and heat transfer performance over fractal surfaces and try to establish it's relation with the fractal dimension of the surface. Additionally, for a surface with the same fractal dimension we will also randomize the arrangement of the cuboids to analyze the similarities and differences in the turbulent flow & heat statistics. The simulations will be conducted using Direct Numerical Simulations (DNS) which integrates the Navier-Stokes equations without any tuning or modelling assumptions. We simulate the heat transfer as a passive scalar and neglect the effect of buoyancy in the flow. For simulating the effect of cuboids we will use an Immersed boundary method designed by Pourquie *et al.* [1] which is very suitable for cubical shaped obstacles and also make the computational domain parallel in the x-direction. Finally, we will be using periodic boundary conditions in the stream-wise direction which is analogous to simulating fully developed flows [26]. The objectives of this thesis will be presented in the next subsection.

1.4. Objectives

From the literature study done above, we limit the objectives of the current thesis to the following goals:

1. Develop a Fortran code to simulate heat transfer of a turbulent channel flow over a fractal surface using an Immersed boundary method and make it parallel in the x-direction.
2. How do the different random realizations affect the flow hydrodynamically? What is the difference within the same fractal dimension?
3. What is the averaged effect of increasing the fractal dimension of a surface on the heat transfer performance relative to the pressure drop?

1.5. Outline of thesis

- Chapter 2 provides a basic introduction about fractals in general and presents a detailed explanation of the methodology employed to design the fractal surfaces for the current study.
- Chapter 3 gives an insight into the Direct Numerical Simulations setup used in this thesis. It also briefly explains the immersed boundary method used to simulate the cubical obstacles and the methodology used to make the model parallel in the X-direction.
- Chapter 4 discusses the results of the current thesis. Initially, a summary of the roughness cases simulated in the current study along with the methodology for post processing the results is presented. This is followed by roughness length estimations for the two kinds of fractal surfaces and ultimately the enhancement of heat transfer relative to pressure drop is analyzed with respect to the fractal dimension of the surface.
- Chapter 5 presents various conclusions drawn from chapter 4 and several recommendations for further studies are made.

2

Design of fractal surface

In this chapter, a basic introduction of fractal geometry will be provided along with it's properties followed by a detailed description of the method used to design fractal surfaces for the final simulations.

2.1. Introduction to fractals

The theory of fractals which is one of the most important developments in natural science was firstly introduced by Mandelbrot [29]. It was derived mainly to overcome the shortcomings of classical geometry in describing the structural disorder and chaos of naturally occurring complex shapes and phenomena. Fractal geometry finds applications in numerous fields ranging from molecular physics to the large scale structure of the universe, and provides new conceptual tools and insights [5]. Numerous examples of fractal objects can also be observed in our daily environment like the shapes of coastlines, clouds, and mountains etc. A very interesting and unique property of fractal objects is that with increased magnification, increasing details of the object keep appearing. These details tend to follow the same structural pattern at several length scales of observation [30].

In classical Euclidean geometry, the shapes of smooth structures are characterized by dimensions having integer values like line (1 dimension), square (2 dimension) etc. and hence it fails to completely characterize the structural complexity found in numerous natural objects. In order to tackle this, Mandelbrot extended the classical definition of a dimension to include a fractional value which provides a measure for the space filling capacity of a complex rugged structure. The idea was to differentiate between the topological dimension of a system and its fractal dimension. By topology, we mean that the properties of a system remain invariant when the space in which they are contained is distorted [5].

An example of the same is shown in figure 2.1 where different shapes of curves have varying space filling capacities. The topological dimension of all curves is one because if suppose all the curves were to be drawn on an elastic graph, when the graph is stretched all the curves will fit over a traditional straight line whose topological dimension is one. However, the fractal dimension of the curves will lie between one and two as the respective space filling capacity of each curve is more than a line but less than a plane. Another example can be that of a paper surface which under normal human vision is perceived as a flat, straight, and Euclidean surface whose topological dimension is two. Nevertheless, when the paper is magnified more details of the roughness structure appear which cause a variation in its fractal dimension. Therefore the use of fractal dimensions provides a new tool for describing such roughness [5]. Additionally, it is easily apparent that Euclidean shapes are usually described by a simple algebraic formula, whereas fractals are the result of a recursive construction procedure or algorithm [5]. In our current application, fractal shapes designed in section 2.2.1 will also be made

recursively leading to algebraic relations between properties and length scale.

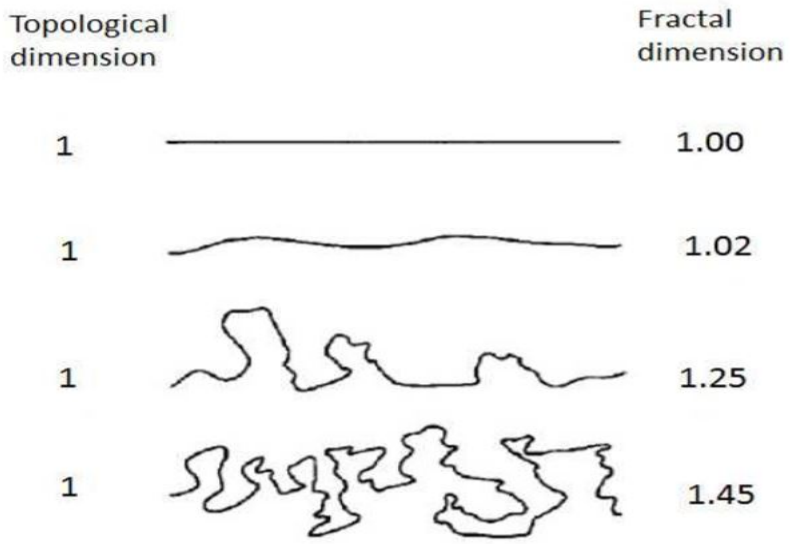

Figure 2.1: Difference between topological dimension and fractal dimension. The space filling capacity of each curves increases from top to bottom and hence the increase in the fractal dimension. [5]

2.1.1. Fractal Dimension

Fractals are characterized by a fractal dimension D. It is defined through covering the fractal with covering elements (line for fractals in one dimension, squares for fractals that live in two dimensions, cubes for the three-dimensional case, etc) and measuring the length (one dimension), area (two dimensions) or volume (three dimensions) with the total number of covering elements.

Fractal dimension is the relation between the total number of covering elements and their linear size. If l is the linear size of a covering element (for squares the side length), and $N(l)$ the number of elements needed to cover the fractal, the fractal dimension D follows from

$$N(l) \sim l^{-D}. \tag{2.1}$$

We will be using this definition to define our fractal surfaces where we cover the planar view of our rough surface with square shaped covering elements to calculate the fractal dimension D which will be described further in section 2.2.1.

Many refinements of this simple notion are possible, for example, we may allow for the different "mass" of the objects that we cover. Another way to understand fractal dimension is asking what the chances $P(l)$ are to find a non–empty square of the fractal cover in 2 dimensions. It is

$$P(l) \sim l^{2-D} \tag{2.2}$$

It is analogous to the above in 3 dimensions.

2.1.2. Self Similarity

The definition of self-similarity is based on the property of equal magnification in all directions [30]. An intuitive example of self-similarity is illustrated in figure 2.2. An object considered as one dimensional possesses a single scaling property in that direction. It can be divided into N identical parts each of which is scaled down by the ratio $l = 1/N$ from the whole. Similarly, a two-dimensional object, such as a square area in the plane, can be divided into N self-similar parts each of which is scaled down

by a factor $l = 1/N^{1/2}$. A three-dimensional object like a solid cube may be divided into N little cubes each of which is scaled down by a ratio $l = 1/N^{1/3}$. With self-similarity the generalization to fractal dimension is straightforward as shown in the above section. A D-dimensional self-similar object can be divided into N smaller copies of itself each of which is scaled down by a factor l where $l = 1/N^{1/D}$.

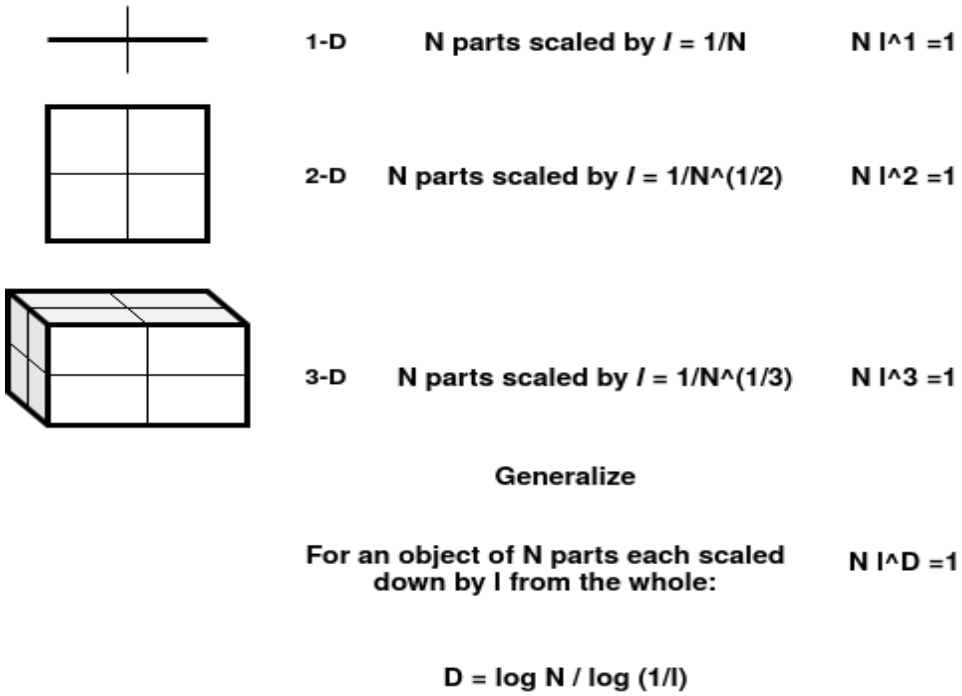

Figure 2.2: Self-similarity concept based on Euclidean objects (line, square, cube). Reproduced from [5]

So far we saw simple Euclidean objects with integer values for fractal dimensions, however for more complex cases the fractal dimension need not be an integer. A simple example of a self-similar complex structure is the Koch curve as shown in figure 2.3 which is constructed by means of a recursive procedure. Firstly, a straight line is broken into three parts and the middle segment is replaced by two segments of equal length. Further, each straight segment is again broken into three parts replacing the middle portion by two more parts and the procedure is repeated infinite times to obtain the Koch curve. Its fractal dimension is $D = \log N / \log(1/l) = \log 4 / \log 3$ or about 1.26. This non integer dimension represents the unusual space filling property of the curve which is greater than simple line ($D = 1$), but less than a Euclidean area of the plane ($D = 2$). Unlike Euclidean shapes, this curve has detail on all length scales. Indeed, the closer one looks, the more detail one finds. More importantly, the curve possesses an exact self-similarity. Each small portion can reproduce exactly a larger portion [5].

2.1.3. Self-affine fractals

Self–affine fractals have the property that there are different scale factors in different directions, not just a single scale factor. A striking example in x, y is the Weierstrass function,

$$y = R(x) = \sum_n \frac{\cos(2\pi\gamma^n x)}{\gamma^{(2-D)n}}, \quad \text{with } \gamma > 1 \tag{2.3}$$

When the horizontal scale changes by a factor γ, the vertical scale changes by a factor γ^{2-D}. This is the key point of self-affinity. When the sum over n extends to ∞, there is no smallest scale. In practical cases, such as for our fractal cover, there is a largest n, and thus a smallest scale. Then, scaling is only observed over a finite dynamical range of length scales.

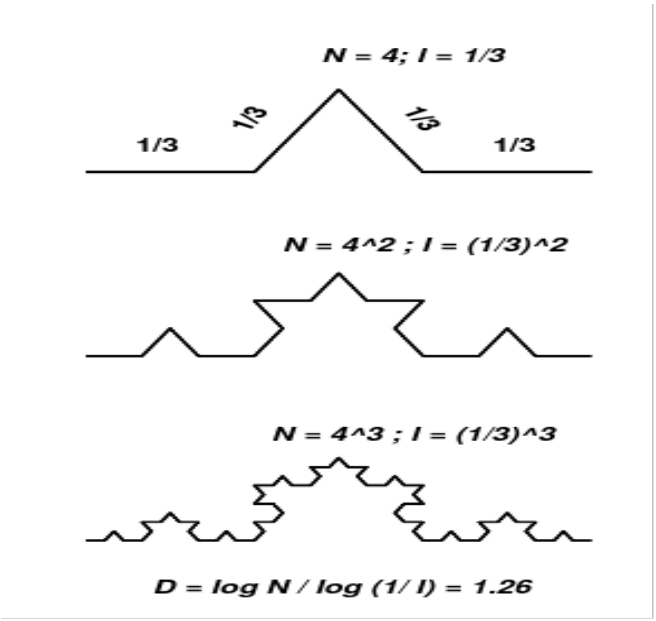

Figure 2.3: Recursive construction of the Koch curve with fractal dimension, D=1.26.

It is easy to see that D in Eq. 2.3 is indeed the fractal dimension: the chances to find a point of the curve in a box with size γ are γ^{2-D}. So, unlike Majumdar and Tien [30], who claim that box–counting dimension does not apply to self–affine fractals, D in Eq. 2.3 is just the box counting dimension.

Self–affine fractals can be characterized by the structure function, which is defined as

$$S_2(x) = \left\langle (R(y+x) - R(y))^2 \right\rangle \simeq x^{2(2-D)} \tag{2.4}$$

The scaling of the structure function trivially follows from Eq. 2.3, and thus caries over to any self–affine fractal.

The scaling exponent ξ of the structure function, $R(x) \sim x^{\xi}$, with $\xi = 2(2 - D_{\mathrm{emb}})$ where D_{emb} is the embedding dimension (2 in this example) does only hold for self–affine fractals. In general, other relations exist between scaling exponent and fractal dimension. A quite relevant example is turbulence.

2.2. Fractal Roughness

Measurements of rough surfaces show that they contain roughness features at several length scales ranging from millimeters to nano-meters [30]. The standard ways to characterize these surfaces is through the root-mean-square variation of the height, the probability density function of elevations, and through the solidity. The solidity λ is defined as the ratio of the area projected along the surface normal to the area projected perpendicular to the surface normal. The idea of fractal scaling can provide an alternative way to characterize rough surfaces which we will try to explore in this thesis.

2.2.1. Making fractal surfaces

We make fractal surfaces by placing prisms with a distribution of sizes. This distribution is fractal, it has a fractal dimension D, but it is not a self–affine fractal.

The prisms come in generations n. In generation n, the size of the square ground plane of a prism is $L_n \times L_n$, whereas the height is $L_n/2$. In this way we follow Yang and Meneveau [4]. The sizes are $L_n \sim \beta^{-n}$, their numbers are $N_n \sim \beta^{\alpha n}$. Trivially, the fractal dimension of the vertical projection of this rough surface is $D = \alpha$ since $N_n \sim L_n^{-\alpha}$. For the case $\alpha = 2$, which was done by Yang and Meneveau

[4], $D = 2$, so their surface was not fractal.

Figure 2.4 shows the top view of two fractal surfaces, one with $D = \alpha = 1$, the other one with $D = \alpha = 2$. These dimensions were verified by covering the top view with a regular grid with mesh size δ, and counting the number $N(\delta)$ of non-empty cells. Figure 2.4 (c) demonstrates that the fractal scaling, observed over a limited dynamical range of scales δ, is consistent with the construction.

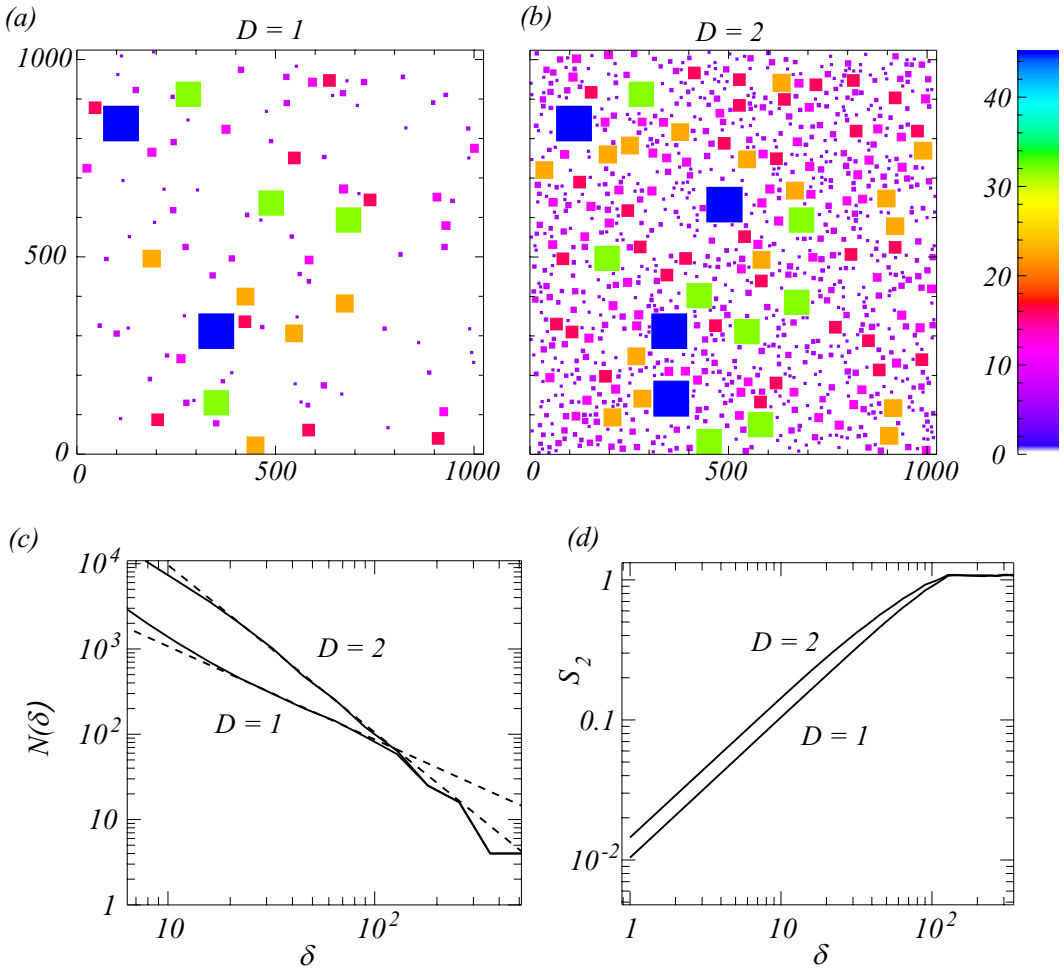

Figure 2.4: Fractal rough surfaces generated by randomly sprinkling prisms on a 1024×1024 grid, with side length of ground plane $L_n = L_0\beta^{-n}$, height $L_n/2$, number $N_n = N_0\beta^{\alpha n}$, with $\beta = 2^{1/2}$, $L_0 = 170$ and $N_0 = 2$. The generations n ranged from $n = 2$ to $n = 8$. (c) Covering with a regular grid with mesh size δ and counting the number $N(\delta)$ of non-empty cells. The dashed lines have slopes -2 and -1 for $D = 2$ and $D = 1$, respectively. (d) Structure functions $S_2(\delta)$.

Our fractal surface is not self-affine, and has a trivial correlation function $S_2(x)$. It is easy to see that each generation n adds a linear piece $S_2(x) \sim x$ to the correlation function which simply follows from the used rectangular building blocks of the rough surface. This is illustrated in figure. 2.4 (d).

The fractal surface of figure. 2.4 was constructed on a 1024×1024 grid by choosing cubes with size $L_n = L_0\beta^{-n}$ and height $L_n/2$. At each generation the number of cubes is $N_n = N_0\beta^{\alpha n}$, with α the fractal dimension. The generations n, ranged from $n = 2$ to $n = 8$, with $L_0 = 170$, $N_0 = 2$ and $\beta = \sqrt{2}$. At each new generation n, N_n cubes with size L_n were sprinkled randomly in the space left by the previous generations. Consequently, the number of generations is limited, with the available space decreasing more rapidly as D increases.

For our fractal roughness the structure function cannot be used to distinguish one fractal surface from another one. Other ways to characterize rough surfaces are the root-mean square height ($\sigma = \langle (h - \langle h \rangle)^2 \rangle^{1/2}$), and the solidity. The solidity λ is defined as the surface area of the $X-$ (or $Y-$)

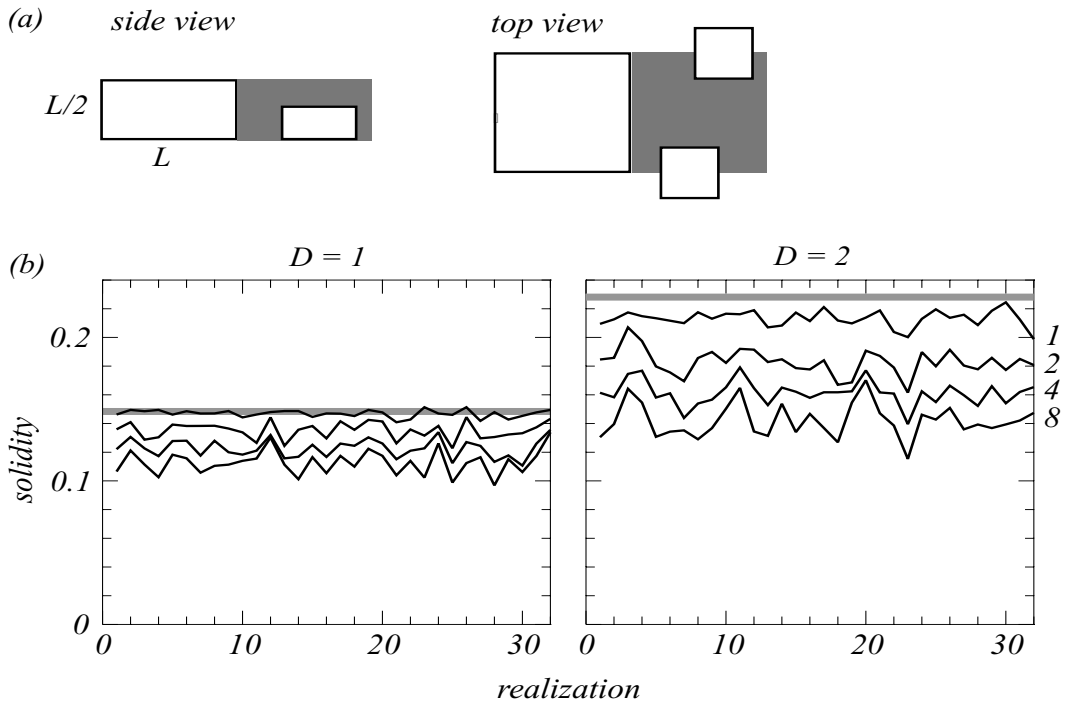

Figure 2.5: Solidity of randomly generated fractal surfaces on a 256×256 grid, taking into account geometric sheltering of small prisms by large ones. (a) Sheltering is the case when a smaller prism sits in the shade of a larger one. The length of the shade is varied from $L, 2L, 4L, 8L$. The prisms drawn are sheltered, their frontal area does not contribute to the total solidity of the surface. (b) In the random generation of fractal surfaces, the dimension is kept constant, but the fluctuating distribution of prisms results in a fluctuating solidity. The gray lines are the solidity without considering sheltering.

projection of all prisms over the total planar area. In principle, both quantities σ and λ can be computed analytically. For $D = 2$, we have, in our realizations, $\sigma = 12.1$ and $\lambda = 0.19$. For $D = 1$, we have $\sigma = 8.4$ and $\lambda = 0.042$. Although, the rms heights σ, for the two surfaces of figure. 2.4 are not very different, the relative fluctuating heights are $\sigma/\langle h \rangle = 1.6$ for $D = 2$, and $\sigma/\langle h \rangle = 3.7$ for $D = 1$. Therefore, the rms height σ is not a good quantity to distinguish the two rough surfaces at $D = 1$ and $D = 2$. Better quantities are the relative fluctuating height $\sigma/\langle h \rangle$, the solidity (σ), and, of course the fractal dimension D.

Alternatively, it is interesting to consider the probability density function $P(h)$ of height h variations. Also, $P(h)$ can be computed analytically: it is flat for $D = 2$ and $P(h) \simeq h$ for $D = 1$. Therefore, it is very different from that of self–affine surfaces (for example surfaces based on Eq. 2.3) which have a near–Gaussian PDF.

In the random generation of fractal surfaces, the dimension is kept constant between different realizations of the surfaces. However, when we allow for sheltering of small prisms by large ones upstream, the fluctuating distribution of prisms results in a fluctuating solidity. These fluctuations will be more prominent for smaller grids. We consider a simple geometric model, in which we vary the downstream length of the shadow. The results are shown in figure 2.5.

The final fractal surface designed for simulations with $D = 1$ & $D = 2$ were constructed on a 256×256 grid unlike the 1024×1024 grid shown in figure 2.4 and details of those cases will be provided in section 4.1.

3

Numerical model

In this chapter, the details of direct numerical simulations method employed for the study are discussed. A brief description of the finite volume method, details on the grid and boundary conditions along with the stability criteria are given. This is followed by a description of the immersed boundary method for cubical obstacles and the implementation of the parallel model.

3.1. Direct Numerical Simulations

In Direct Numerical Simulations (DNS), the Navier-Stokes equations are solved by resolving all the scales of motion (from largest to smallest eddies), with the initial and boundary conditions relative to the flow requirements. This approach does not employ any modelling approximations (unlike LES & RANS) and hence it is known to give very accurate and detailed results about the flow which also makes it computationally very expensive. However, to ensure that the DNS resolves both the macro and micro-structures of turbulence, the flow domain must be large enough to contain the large-scale motions of size $\mathcal{L}$, while at the same time the spatial resolution Δ of the grid should be small enough to resolve the Kolmogorov scale η. Using the above length scales, an estimation can be made of the total number of grid cells $\mathcal{N}$ in the simulation:

$$\mathcal{N} \approx \left(\frac{\mathcal{L}}{\eta}\right)^3 = \mathcal{O}(Re^{9/4}) \tag{3.1}$$

Additionally, the integration time step Δt should be small enough to resolve the Kolmogorov timescale τ_η, while the total simulation time should be sufficiently long to cover a sufficient number of integral timescales $\mathcal{T}$. It can be shown that:

$$\frac{\mathcal{T}}{\tau_\eta} \sim Re^{1/2} \tag{3.2}$$

Hence an estimation for total number of computations required can be scaled according to:

$$\mathcal{N}x\mathcal{M} = \mathcal{O}\left(Re^{9/4}.Re^{1/2}\right) = \mathcal{O}\left(Re^{11/4}\right) \tag{3.3}$$

where $\mathcal{M}$ is the total number of time integration steps. Thus, it can be seen that the computational effort of DNS grows almost with an exponent of three of the Reynolds number. In view of such high

computation costs it's applicability is limited only to flows with low or moderate Reynolds numbers [9] [10]. However, various engineering estimates could be made on the maximum domain size and the smallest grid size (where it need not be exactly equal to the Kolmogorov scale but in order of magnitude of the same).

In the present study, an in-house code developed by Boersma & Pourquie which uses a finite volume approach for solving the Navier-Stokes and the energy equation has been modified further to include a random array of multi-sized cubes (using IBM [1]). In the next sub-section, the basic flow and energy equations are described.

3.1.1. Basic equations of fluid flow

Fluid flow is described using three sets of equations, namely, conservation of mass, Eq. 3.4, conservation of momentum, Eq. 3.5 & the conservation of energy, Eq. 3.6. The flow is considered to be incompressible in the present research and there are no internal sources of heat within the fluid. Also, the temperature is modelled as a passive scalar (i.e temperature variations do not affect the momentum equation). The equations are given as below:

$$\frac{\partial u_i}{\partial x_i} = 0 \tag{3.4}$$

$$\rho_f * (\frac{\partial u_i}{\partial t} + \frac{u_j \partial u_i}{\partial x_j}) = -\frac{\partial p}{\partial x_i} + \mu \frac{\partial^2 u_i}{\partial x_i^2} \tag{3.5}$$

$$\rho_f C_p (\frac{\partial T}{\partial t} + \frac{u_j \partial T}{\partial x_j}) = \lambda (\frac{\partial^2 T}{\partial x_j^2}) \tag{3.6}$$

In fluid mechanics, it is a preferred practice to make the above equations non-dimensional using relevant flow and geometric scales. Dimensionless equations give a better insight on the dominating terms in the Navier-Stokes and energy equations thereby highlighting the importance of certain forces. Also, using non-dimensional equations helps us in up-scaling or down-scaling experimental setups for similar physical situations. Non-dimensionalization can be done using characteristic velocity, length, time and temperature scales relevant to the problem. In our case we do it with respect to the channel height (H), bulk velocity ($\mathcal{U}_b$) and temperature difference between the hot and cold wall ($T_h - T_c$).

$$u^* = \frac{u}{\mathcal{U}_b}, \quad x^* = \frac{x}{H}, \quad t^* = \frac{t.\mathcal{U}_b}{H}, \quad T^* = \frac{T}{(T_h - T_c)} \tag{3.7}$$

Substituting the above into Eqs. 3.4, 3.5 & 3.6 we get the following

$$\frac{\partial u_i^*}{\partial x_i^*} = 0 \tag{3.8}$$

$$\frac{\partial u_i^*}{\partial t^*} + \frac{u_j^* \partial u_i^*}{\partial x_j^*} = -\frac{\partial p^*}{\partial x_i^*} + \frac{1}{Re_b} \frac{\partial^2 u_i^*}{\partial x_i^{2^*}} \tag{3.9}$$

$$\frac{\partial T^*}{\partial t^*} + \frac{u_j^* \partial T^*}{\partial x_j^*} = \frac{1}{Re_b Pr} \frac{\partial^2 T^*}{\partial x_j^{2^*}} \tag{3.10}$$

From the above equations, we see that two important non-dimensional terms emerge, namely, the bulk Reynolds number Re_b and the Prandtl number Pr. They can be expressed as follows:

$$Re_b = \frac{\mathcal{U}_b H}{\nu}, \quad Pr = \frac{\nu}{\alpha} \tag{3.11}$$

3.1.2. Staggered grid

In order to discretize the Navier-Stokes equations in three dimensional space, the continuous spatial domains must be divided into a set of discrete cells or control volumes over which the physical flow quantities are stored. In the present simulation, a staggered grid is used where the scalar quantities are stored at the cell centers and vector quantities are stored at the cell edges (figure 3.1). This setup prevents the odd-even decoupling between pressure and velocity which is seen in collocated grids [6].

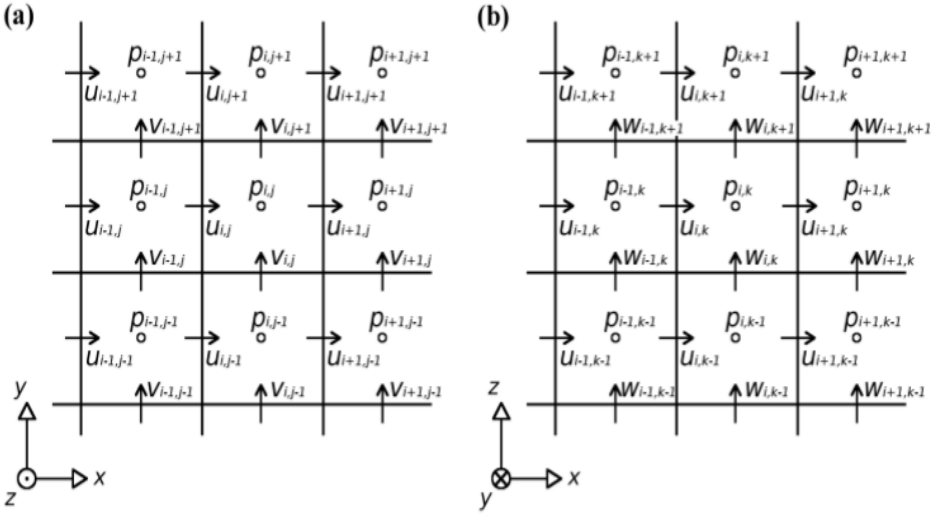

Figure 3.1: Staggered grid with velocities u, v, and w evaluated at the cell faces, while scalars like pressure and temperature (only p shown) are evaluated at the cell centers indicated by the circles. The relative position of the cells is indicated by the indices i, j, and k. (a) grid in the x−y plane, (b) grid in the x-z plane. Reproduced from Tomas [6]

3.1.3. Spatial Discretization

The spatial derivatives for Equations 3.8 & 3.9 (continuity and momentum equation) are discretized using a second-order central difference scheme. For Equation 3.10 (energy equation) however, the convective term is discretized using a second-order upwind scheme (kappa scheme Hundsdorfer *et al.* [32]) and the diffusion term is discretized using a second-order central difference scheme to ensure physical positive values at the domain boundaries. All the discretizations done, ensure that the mass, momentum and energy are conserved over the control volume. The grid spacing is maintained uniform in all the three directions without any grid stretching as we need to model multiple scales of cubes.

3.1.4. Time Integration and Pressure-Correction Method

Integration in time is done by marching equations 3.9 & 3.10 over a time step Δt by using an explicit scheme as implicit schemes will be computationally very expensive. For the momentum equation we use a second order Adams Bashforth scheme but for the energy equation we use a third order TVD Runge Kutta Scheme (Gottlieb and Shu [33]) where the latter is mostly used along with higher order spatial discretization schemes mentioned above to ensure physically positive values. The integration step for the scalar (temperature equation 3.10) is very straight forward and the new time integrated

value satisfies the energy balance over the control volume cell. However, the same cannot be said about the velocity which does not satisfy the continuity equation 3.8. This happens because in the momentum equation (equation 3.9) there is no time derivative for the pressure. However, this issue can be solved by using a fractional step method to correct the velocities and pressure at each time step. We describe the procedure in terms of the second order Adam Bashforth scheme which we use for time integration of the momentum equation.

$$\frac{u^{n+1}-u^n}{\Delta t} = -\nabla p^n - \nabla \tilde{p} + \frac{1}{2}\Big(3(-\mathcal{A}_n + \mathcal{D}_n) - (-\mathcal{A}_{n-1} + \mathcal{D}_{n-1})\Big) \tag{3.12}$$

The terms $\mathcal{A}$ & $\mathcal{D}$ represent the advection and diffusion terms respectively of the momentum equation 3.9 and $\tilde{p}$ is the pressure correction term. Initially, an intermediate value of velocity called the prediction velocity, u^p is calculated as shown in Equation 3.13 which is not divergence free. Taking the divergence of equation 3.13, we get equation 3.14 that can be solved using a fast Poisson solver to obtain the pressure correction $\tilde{p}$ which can be used to correct the final velocity and pressure at the new time step as shown in Equation 3.15 & 3.16.

$$u^p = u^n + \Delta t\Big(- \nabla p^n + \frac{1}{2}\Big(3(-\mathcal{A}_n + \mathcal{D}_n) - (-\mathcal{A}_{n-1} + \mathcal{D}_{n-1})\Big)\Big) \tag{3.13}$$

$$\nabla^2 \tilde{p} = \frac{1}{\Delta t}(\nabla . u^p) \tag{3.14}$$

$$u^{n+1} = u^p - \Delta t(\nabla \tilde{p}) \tag{3.15}$$

$$p^{n+1} = p^n + \tilde{p} \tag{3.16}$$

3.1.5. Stability Condition on time step

Explicit time integration schemes have a disadvantage over their implicit counterpart due to the restriction on the largest allowable time step size required for stability. The two important stability criteria that govern the maximum time step size are stated below. The first criterion, is the Courant-Friedrichs-Lewy (CFL) condition;

$$\Delta t(\frac{u}{\Delta x} + \frac{v}{\Delta y} + \frac{w}{\Delta z}) \leqslant C_{max} \tag{3.17}$$

where C_{max} is the maximum Courant number. We maintain C_{max} below 0.3 for our simulations. The second criterion is that of the diffusion number whose critical value is maintained below 0.4 given as [6].

$$\text{Diffusion number} = \frac{\alpha \Delta t}{(\Delta x^2 + \Delta y^2 + \Delta z^2)} \tag{3.18}$$

where α stands for the scalar diffusivity. The above criterion also holds for the diffusion of momentum where the diffusivity, α can be replaced by viscosity, ν.

3.1.6. Domain Setup & Boundary Conditions

The domain size for the fractal case simulations is scaled according to the length of the largest generation of cubes ($\mathcal{L}$). In the three directions, we have the domain size as $6\mathcal{L}$ x $6\mathcal{L}$ x $6\mathcal{L}$ and a uniform resolution of 256 x 256 x 256 is set.

Also in order to solve the flow equations, it is essential to provide proper boundary conditions. In the stream wise (x) and lateral (y) directions we use periodic boundary conditions for velocity. At the top wall (smooth) and bottom wall (fractal cubes) we use a no slip boundary condition. For the scalar temperature we provide a constant temperature at the inlet ($T = 5$) and a robust convective boundary condition at the outlet in the stream wise (x) direction. Iso-thermal wall conditions are used on the top (cold, $T = 0$) and bottom wall (hot, $T = 10$) and the lateral (y) direction boundaries are periodic. The convective outlet boundary condition for the scalar can be given as below:

$$\frac{\partial T}{\partial t} + \mathcal{U}_b \frac{\partial T}{\partial x} = 0 \tag{3.19}$$

where T indicates the temperature and $\mathcal{U}_b$ is the bulk velocity. The scheme used for the time integration of this boundary condition is the third order TVD Runge Kutta scheme which is the same as for the scalar equation 3.10. The computational domain is represented below in figure 3.2 with relevant boundary conditions.

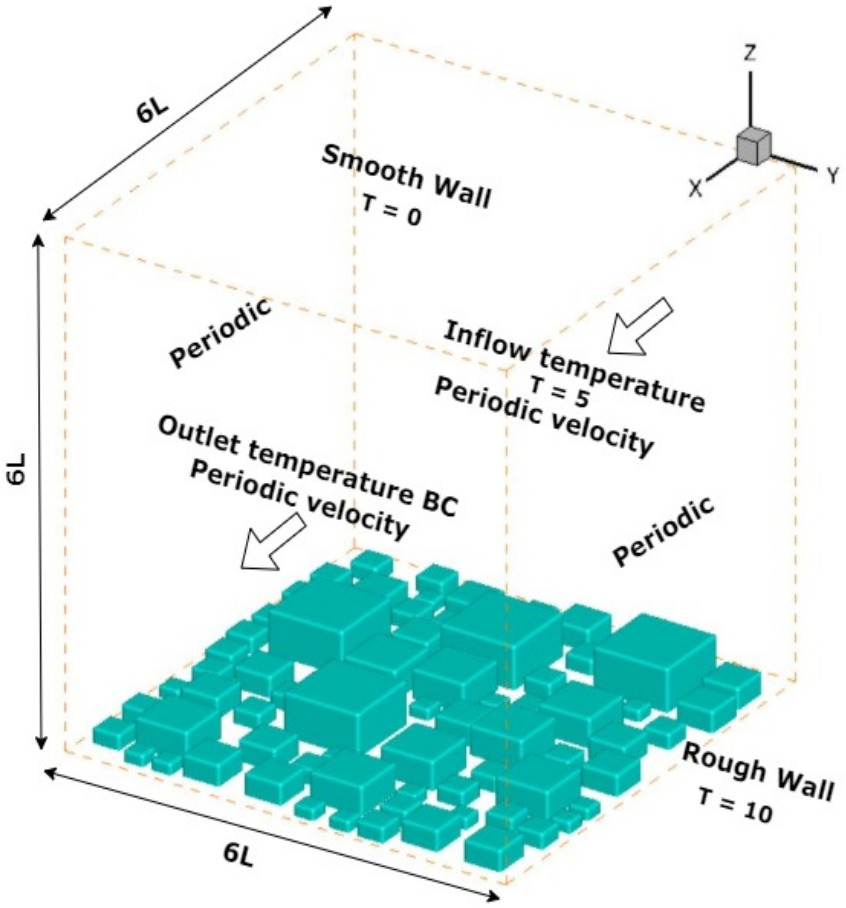

Figure 3.2: An illustration of the domain used in the simulation (One case with fractal dimension $D = 2$). The top wall is smooth with $T = 0$ & the bottom wall contains the fractal cubes with $T = 10$. In the stream wise (x) direction we have periodic boundaries for velocity and inflow/outflow for temperature. The lateral (y) boundaries contain periodic conditions for velocity and temperature. The dotted lines represent the edge of the computational domain and the shaded surfaces at the bottom wall represent the fractal cubes.

In order to sustain the flow in the stream wise direction which uses periodic boundaries we need to implement a forcing strategy which is mentioned in the next section.

3.1.7. Forcing strategy used for periodic boundary condition

For a flow to occur through a channel/pipe, an external source of energy is usually required that supplies the pressure gradient across the stream wise channel to overcome the friction losses occurring at the walls. In experimental channel flow studies, the driving force is generated mostly by means of a pump. However, in numerical simulations especially with the ones having periodic boundary conditions in the stream wise direction an additional modelling step to define the external force is necessary. There are two methods by which this forcing term can be defined, namely, the constant flow rate and the constant pressure gradient method. In the constant flow rate method, the force required to maintain a constant mass flow rate along a cross-section of the channel is calculated and adjusted uniformly at all cells in the entire channel at every time step excluding the cells inside the fractal cubes on the bottom wall. When defining the forcing term with the constant flow rate method, it is easy to define the Reynolds number in terms of channel height (H) and the bulk velocity ($\mathcal{U}_b$).

$$\mathcal{U}_b = \frac{1}{H}\int_0^H u dy \tag{3.20}$$

$$Re_b = \frac{\mathcal{U}_b H}{\nu} \tag{3.21}$$

In the constant pressure gradient method, the external driving force is prescribed by setting a constant value of pressure gradient at all cells uniformly (except the cells in the fractal cubes) throughout the domain in the x-component of the momentum equation. This constant pressure gradient balances the shear stress (τ_w) at the walls. When using this method, the flow is specified through friction Reynolds number defined in terms of the channel height and the friction velocity (u_τ).

$$u_\tau = \sqrt{\frac{\tau_w}{\rho}} \tag{3.22}$$

$$Re_\tau = \frac{u_\tau H}{\nu} \tag{3.23}$$

In the current thesis, the constant flow rate approach is used to define the external driving force.

3.2. Immersed Boundary Method

In this thesis, we incorporate cubes in the flow domain by using an Immersed boundary method wherein the cubes will be immersed in the three-dimensional flow computational grid with appropriate wall forces applied on the fluid rather than imposing no-slip / no-penetration conditions at the fluid solid interfaces. The main advantage of this method is that a regular continuous grid without any holes in the flow domain could be used which enables the use of an efficient FFT based direct solver to evaluate pressure correction from the Poisson equation 3.14 [34]. We will be using an IBM method by Pourquie *et al.* [1] which is very suitable for simple geometries (cubical structures) and produces accurate results when computing flow over cubical objects. In this technique, the cubes are aligned along the computational mesh in such a way that it's surface coincides with the mesh points for the normal velocity location as shown in figure 3.3. This allows for an exact implementation of the wall boundary conditions on the fluid.

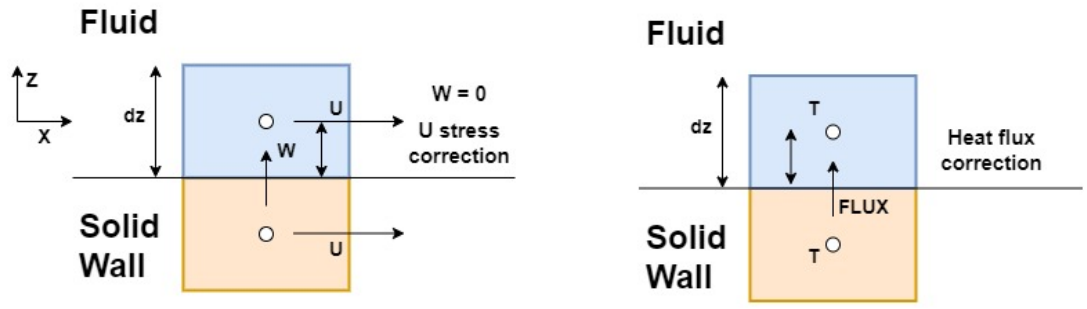

Figure 3.3: A representation of the stress IBM method by Pourquie *et al.* [1]. (Left) Velocity treatment at cube wall. Normal velocity is set to zero before pressure correction. For tangential velocity, the contribution from the stress at the bottom fluid cell face, calculated as if no wall is there, is subtracted and a new stress is added which uses a no-slip condition for the tangential component. (Right) Scalar treatment at cube wall. The contribution by the scalar flux at the bottom cell wall as if no wall is there is subtracted and the scalar flux for a wall is added.

The no-penetration condition on the cubes is enforced by putting the prediction velocity w^p at the wall location to zero (as shown in figure 3.3). However, the pressure correction step may cause these penetration velocities at the cube surfaces to be $w^p \neq 0$ but these values are restricted to the order of $10^{-4}\mathcal{U}_b$ in the current simulations. Similar treatment is applied for u^p & v^p on cube walls which have normals along the x & y directions respectively. In addition to this, the no-slip condition can be applied by replacing the shear stress without the wall in the momentum equation 3.9 with the shear stress due to the wall as represented in figure 3.3. For example, in the x-component of the momentum equation 3.9 the diffusion part can be given as:

$$\mathcal{D} = \frac{\partial}{\partial x}\Big[\nu\Big(\frac{\partial u}{\partial z} + \frac{\partial w}{\partial x}\Big)\Big] \tag{3.24}$$

The above equation can be discretized as follows at the point (i, j, k):

$$\mathcal{D} = \frac{1}{\Delta z}\Big[\nu\Big(\frac{u^{i,j,k+1} - u^{i,j,k}}{\Delta z} + \frac{w^{i+1,j,k} - w^{i,j,k}}{\Delta x}\Big) - \nu\Big(\frac{u^{i,j,k} - u^{i,j,k-1}}{\Delta z} + \frac{w^{i+1,j,k-1} - w^{i,j,k-1}}{\Delta x}\Big)\Big] \tag{3.25}$$

For the point above the wall, the part of equation 3.25 which contains the stress for the wall i.e

$$\nu\Big(\frac{u^{i,j,k} - u^{i,j,k-1}}{\Delta z} + \frac{w^{i+1,j,k-1} - w^{i,j,k-1}}{\Delta x}\Big) \tag{3.26}$$

is replaced by the actual stress when the wall is present i.e

$$\nu\frac{\partial u}{\partial z}\Big|_{wall} = 2\nu\frac{u^{i,j,k}}{\Delta z} \tag{3.27}$$

This treatment can be translated to other tangential velocities v & w along respective cube walls and it is performed both outside the cube surface and within the cube surface. A procedure similar to the above is carried out for heat flux in the energy equation as shown in figure 3.3. Furthermore, it should be noted that the forcing term from the constant flow rate method described above is set to zero inside the cube.

3.3. Parallel Implementation of model

The above DNS code is made parallel in the stream wise (x) direction. Each sub-domain is solved independently in a particular core on the cluster, with flow & energy data exchange between cores occurring through MPI (Message Passing Interface). We use 16 cores for the final simulations.

The cube boundaries are defined by using index limits in the three directions on the global domain. There are two main sets of indices to define cube boundaries: the global indices (global domain) and the local indices (for each processor). The total count of cubes defined in local indices is equal to the global count. For eg. if there are 44 cubes in the global domain then each local processor will also have 44 local cube indices. When the model is made parallel in the x direction, the cubes are distributed in different processors where the global cube indices are converted to local indices on every processor. The idea behind defining equal local cubes is that after making the model parallel, if the global cubes are not present in a particular local processor then garbage values are stored in those corresponding cube indices. On the other hand if the global cubes are present in a local processor (either completely or partially) then those corresponding local cube indices will be assigned relevant positions ([1]). The IBM routine will only execute for realistic local cube indices and will be discarded for those cubes which contain garbage indices. After the model is made parallel in the x direction, one of the following six interactions of the cube boundary with the processor boundary will be encountered as shown in figure 3.4 (top view of the bottom wall in the computational domain). Therefore, either complete cube indices will be stored in one local processor and garbage values in the other as in cases 1 and 2 or the cubes indices will be split amongst local processors as in cases 3, 4, 5 and 6.

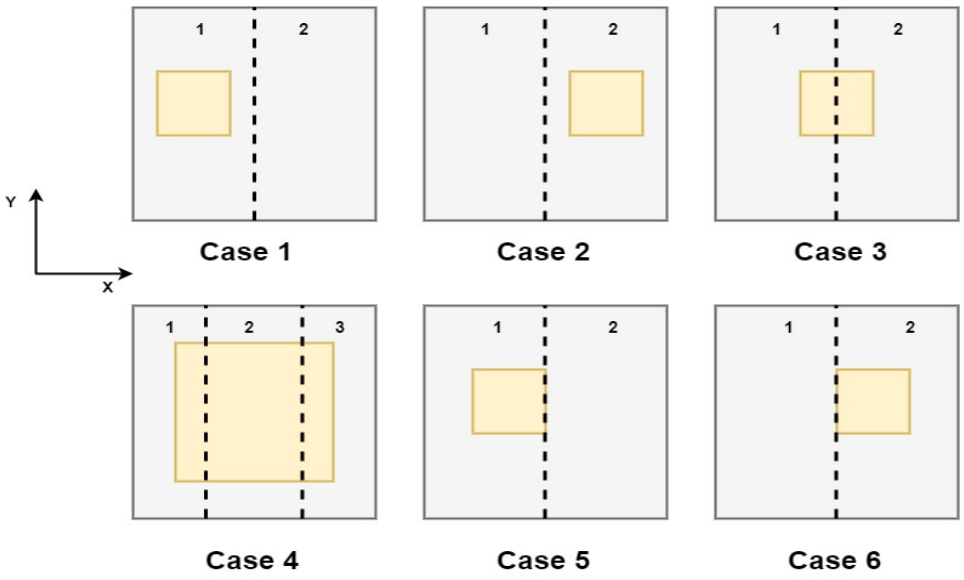

Figure 3.4: A top view of the domain is shown ($x-y$ direction). The domain is made parallel in the stream wise (x) direction. Therefore, when the cubes are divided one of the six cases mentioned above will occur. The external grey rectangle represents the domain in the X-Y plane and the internal yellow square represents the cube. The dotted line represents the processor boundary.

[1]The global cube indices are defined on a grid size of 256 in x direction while the maximum sub-domain index of each processor is 16 in x direction. Hence, the local cube index needs to be adjusted depending on the distance of the processor from the start of the global domain.

4

Results & discussions

4.1. Roughness cases summary and analysis

4.1.1. Fractal rough surfaces

In chapter 2 a brief description of the design of fractal surfaces was provided whereas in chapter 3 the numerical method and boundary conditions for the domain were mentioned. In this section, roughness parameters and details on the case setup is provided along with various results. Different realizations of surfaces with two fractal dimensions were studied, i.e. $D = 1$ & $D = 2$. In principle, a fractal roughness is characterized by self-similar detail on smaller and smaller length scales, however considering the resolution limits and the cost of the simulation the total number of cuboid generations were limited to 5. The size distribution of the cuboids used were same as that mentioned in chapter 2. The cuboids were randomly sprinkled on the bottom surface of the domain (figure 3.2) which gave rise to inhomogeneity for a given fractal dimension. Hence, eight random realizations of each fractal dimension were generated in order to evaluate the averaged effect of the surface fractal dimension on the heat transfer performance. As mentioned in chapter 1, Chen *et al.* [31] conducted a study to probe the effect of the fractal dimension on the heat transfer performance and concluded that the heat transfer is enhanced with increasing fractal dimension. However, the fractal roughness implemented by Chen *et al.* [31] was self-affine, whereas in the present study our distribution of cuboids is self-similar and it is of interest to know if a similar trend is observed for surfaces in the current study too.

An example of different realizations for fractal dimension $D = 1$ is shown in figure 4.1 which was similarly implemented for $D = 2$ as well. Additionally in figure 4.1, the solidity (λ_f) of the surface for various realizations is also shown. Since the cuboids are randomly placed for various realizations they may produce varying sheltering effects for those realizations even though the geometric frontal area is the same. The horizontal line on the top represents the geometric solidity for various realizations, however as can be seen there is more variability in the solidity in the lines below. The flow sheltering considered here is geometric by considering the wake of the cuboids to be of certain length (in terms of cube units) and neglecting the frontal area of the cuboids that fall within the above shelter. The different lines represent a shelter factor of 1, 2, 4 & 8 respectively from top to bottom. Further analysis on the considerations of this shelter factor will be done in section 4.2.4.

As mentioned earlier, the size of the largest generation of cuboid is $\mathcal{L}$ with its corresponding height of $\mathcal{L}/2$ and size of the computational domain is $6\mathcal{L}$ x $6\mathcal{L}$ x $6\mathcal{L}$. All 16 simulations are carried out at a constant bulk Reynolds number $Re_{bulk} = 13000$ ($Re_b = U_{bulk} * 6\mathcal{L}/\nu$, where U_{bulk} is the bulk velocity in channel flow, $6\mathcal{L}$ is the channel height & ν is the viscosity.) and $Pr = 0.71$. As explained in chapter 2, the fractal dimension of our surfaces uniquely determines the solidity and the rms height. For $D = 1$, $\lambda_f = 0.151$ and $h_{rms} = 0.177$ ($h_{rms}/H_{1/2} = 0.059$), where $H_{1/2} = H/2 = 3\mathcal{L}$ is half channel

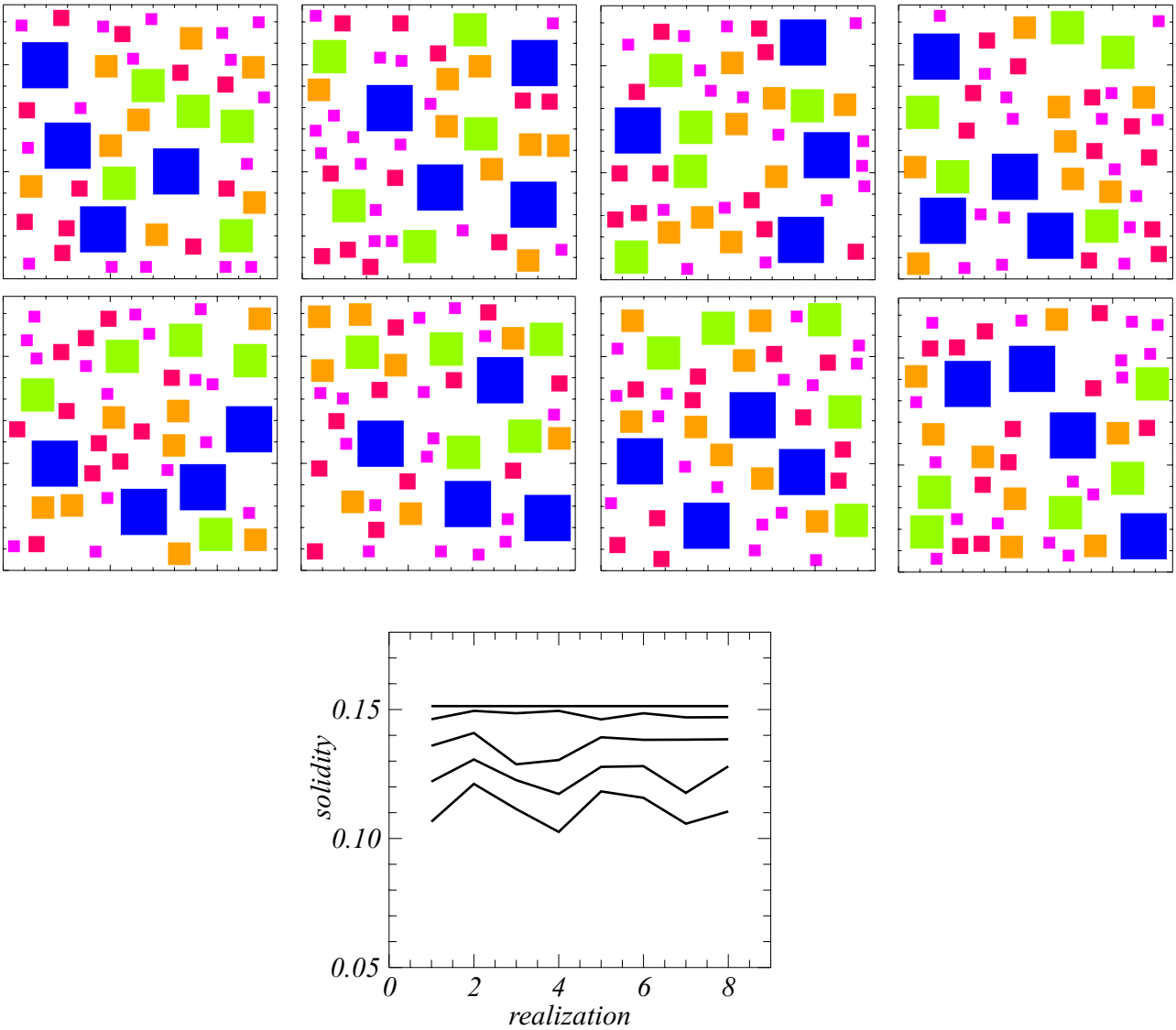

Figure 4.1: An illustration of the top view for 8 random realizations of the fractal surface $D = 1$ used in the study. The color codes represent cuboids of different generations. Also, the solidity (λ_f) of the different realizations are plotted with the top horizontal line representing the geometric solidity and the lines below are solidity with increasing shelter factor (1, 2, 3 & 4).

height & H is the height of the channel. For $D = 2$, $\lambda_f = 0.22 \pm 0.01$ and $h_{rms} = 0.179 \pm 0.001$ ($h_{rms}/H_{1/2} = 0.0597 \pm 0.0001$). It should be noted that the solidity (λ_f) mentioned above is the value presented without sheltering effect i.e it is the geometric solidity.

4.1.2. Methodology for analysis

The objective of this thesis is to understand if the fractal dimension of the surface is a representative parameter for the surface roughness and also if it improves the performance of the surface in terms of heat transfer enhancement. In this section, we describe the methodology implemented for the post-processing calculations of heat transfer and friction parameters for the 16 cases summarized above.

A schematic illustration of the domain setup is given in figure 4.2 and the calculation procedure for bulk flow and heat transfer quantities is inspired by Nagano *et al.* [35] & Forooghi *et al.* [36] wherein the domain is similar to the current setup with roughness elements on the bottom wall and a smooth top wall. Due to the presence of the roughness elements on the bottom wall, the mean velocity profile

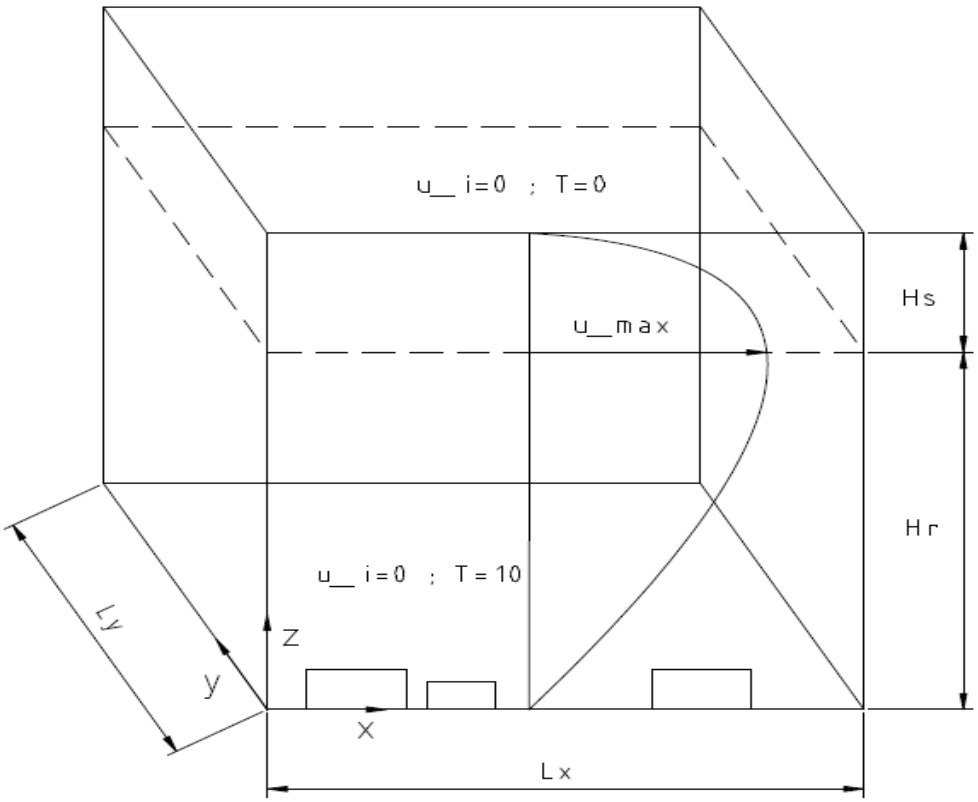

Figure 4.2: Domain for analysis. The volume is divided into two sections based on the maximum velocity location.

over the roughness cases is not symmetric and it's maximum is shifted towards the smooth top wall which will also be seen later in figure 4.3. As depicted in figure 4.2, the channel is split into two parts, namely, the rough wall side H_r and the smooth wall side H_s based on the maximum velocity location ($H = H_s + H_r$). Here, H_r and H_s are determined 'a posteriori' and can be considered as 'effective' channel half height for the rough and smooth sides respectively. The calculation of the bulk quantities along with heat flux and wall stresses are done for the smooth and rough walls based on the above half channel heights as explained below.

Firstly, we focus on the friction losses at the wall. The calculation for the wall shear at the smooth wall is very straightforward.

$$\tau_{w,s} = -\rho\nu\frac{\partial U}{\partial z} \tag{4.1}$$

where U is the velocity averaged in the wall parallel directions and time. The wall stress on the rough side can be calculated by employing a global force balance as shown below.

$$\tau_{w,r} = HP_x - \tau_{w,s} \tag{4.2}$$

Here, $\tau_{w,r}$ is the stress due to both the viscous shear and form drag on the rough wall divided by the total wall projected area. Wall scales namely, friction velocity and viscous length scale for the smooth and rough wall sides can be estimated from above stresses.

$$u_{\tau,s/r} = \sqrt{\frac{\tau_{w,s/r}}{\rho}}, \qquad \delta_{\nu,s/r} = \frac{\nu}{u_{\tau,s/r}} \tag{4.3}$$

Since we mainly study rough wall flows in this thesis, $u_{\tau,r}$ and $\delta_{\nu,r}$ are used for the definition of viscous or plus units $()^+$ unless otherwise stated.

As regards the heat flux, they are calculated respectively at the smooth and rough walls from mean temperature gradients at the fluid-wall interface.

$$q_{w,s/r} = -k_{fl}\frac{\partial T}{\partial z} \tag{4.4}$$

In the above equations, k_{fl} is the thermal conductivity of the fluid.

The surface area considered for the heat flux calculation could either be the wall projected area or the total fluid-wall interaction surface area (i.e total roughness surface area). The wall projected area is considered in studies by Forooghi *et al.* [7] and MacDonald *et al.* [37] etc. while the total surface area is considered in Ventola *et al.* [38] and Lu *et al.* [39] etc. In most boundary layer flows, the projected area of the roughness is considered whereas for compact applications like electronic cooling the total wetted surface area is considered. In the current study, the roughness surface area of $D = 2$ is 1.2 times that of $D = 1$ while the heat transfer from the two surfaces is approximately same. Hence the heat flux is dominated by surface area effects producing significantly higher values for $D = 1$ than $D = 2$ if the total roughness area is considered. However, we are interested in the global heat addition of the surface which can be quantified in terms of a higher global temperature of the fluid in the domain as will be shown in section 4.2.1. The global temperature of $D = 2$ is slightly higher than that of $D = 1$. Hence in order to evaluate the global heat addition from the surfaces, we take the projected surface area for the calculation of the heat flux.

The bulk quantities for velocity and temperature gradients are evaluated for each side by integrating from the wall to the maximum velocity location ($H_{s/r}$).

$$U_{b,r} = \frac{1}{H_r}\int_0^{H_r} U dy, \qquad U_{b,s} = \frac{1}{H_s}\int_{H_r}^{H} U dy \tag{4.5}$$

$$\Delta T_{b,r} = \frac{1}{H_r U_{b,r}}\int_0^{H_r} U(T_h - T) dy, \quad \Delta T_{b,s} = \frac{1}{H_s U_{b,s}}\int_{H_r}^{H} UT dy \tag{4.6}$$

Here, T_h is the temperature of the hot bottom wall.

The friction factor, Nusselt number and the Stanton number can be calculated as,

$$C_{f,s/r} = \frac{2\tau_{w,s/r}}{\rho U_{b,s/r}^2}, \qquad Nu_{s/r} = \frac{4H_{s/r}q_{w,s/r}}{\Delta T_{b,s/r}k_{fl}}, \qquad St_{s/r} = \frac{q_{w,s/r}}{\rho c_p U_{b,s/r}\Delta T_{b,s/r}} \tag{4.7}$$

where, c_p is the heat capacity of the fluid. The length scale used for the definition of Nusselt number is the 'effective hydraulic diameter' which is $4H_{s/r}$ [36]. This because the smooth wall correlations (equations 4.16, 4.17 & 4.18) which are used for normalization of the performance factors are defined based on the 'effective hydraulic diameter'. The plots made for $C_{f,s/r}$ are based on Re_b (bulk Reynolds number) and the plots made for $Nu_{s/r}$ & $St_{s/r}$ are based on Re_{dh} (hydraulic Reynolds number) which are defined as below:

$$Re_{b,s/r} = \frac{U_{b,s/r} H_{s/r}}{\nu}, \qquad Re_{dh,s/r} = \frac{U_{b,s/r} 4H_{s/r}}{\nu} \tag{4.8}$$

The velocity and the temperature fields are averaged over time (denoted by overline $\overline{()}$) after the simulation has reached a statistically steady state which is monitored through the temporal evolution of the drag force and the heat flux over the rough wall. The spatial averaging employed for velocity and temperature fields is carried out in wall parallel directions (denoted by angle brackets <> i.e. $U_i =< \overline{u_i} >$ and $\Theta =< \overline{T} >$) and the averaging is done only in the part of the domain occupied by the fluid an example of which is shown in the formula for the temperature field below.

$$\Theta =< \overline{T} >= \frac{1}{S} \int_S \psi \overline{T} dS \tag{4.9}$$

where ψ is an indicator function that is equal to unity within the fluid and zero in the roughness elements and S denotes the plane parallel to the wall.

Since the goal is to quantify the heat transfer enhancement of rough surfaces and compare it for two types fractal surfaces, a performance factor needs to be defined. It is easily apparent that by increasing the contact surface area of the roughness with the fluid, the heat transfer of the surface will be enhanced however this will also put a penalty on the pump power input (higher pressure drop). Therefore a parameter that finds a balance between both is essential to find an optimal solution. One such parameter is the aero-thermal efficiency (η_a) that was used by Ventola *et al.* [38] which quantifies the heat transfer enhancement of the surface for a given pressure loss.

$$PF_1 = \eta_a = \frac{Nu_{f,r}/Nu_{f,s}}{[C_{f,r}/C_{f,s}]^{1/3}} \tag{4.10}$$

The smooth wall Nusselt number ($Nu_{f,s}$) and skin friction ($C_{f,s}$) have been evaluated at the same bulk Reynolds number as their rough wall counterparts. Another similar parameter which is often used to quantify the rough wall effects is the Reynolds Analogy factor normalized by its value for the smooth wall case Forooghi *et al.* [7].

$$PF_2 = \frac{RA}{RA_0} \tag{4.11}$$

Additionally, the convective heat transfer enhancement due to roughness can also be quantified as below (Ventola *et al.* [38]):

$$E = \frac{Nu_{f,r} - Nu_{f,s}}{Nu_{f,s}} \tag{4.12}$$

4.1.3. Estimation of roughness lengths for fractal surfaces

In the current thesis, several realizations of surfaces with a particular fractal dimension are used with fractal dimension being the representative parameter. Figure 4.3, shows the velocity profiles normalized by the full channel bulk velocity for few cases of the two fractal dimensions. It can be seen that the maxima of the velocity profile is shifted towards the smooth wall side which is indicative of rough wall effects on the flow. Geometrically, the generation of cuboids and height distribution of the generations are the same for different realizations, however due to the randomness in the sprinkling of the cuboids the aerodynamic effect on the flow may not be the same. Therefore, in this section we make an estimate for the aerodynamic roughness lengths for the surfaces studied which quantifies the rough

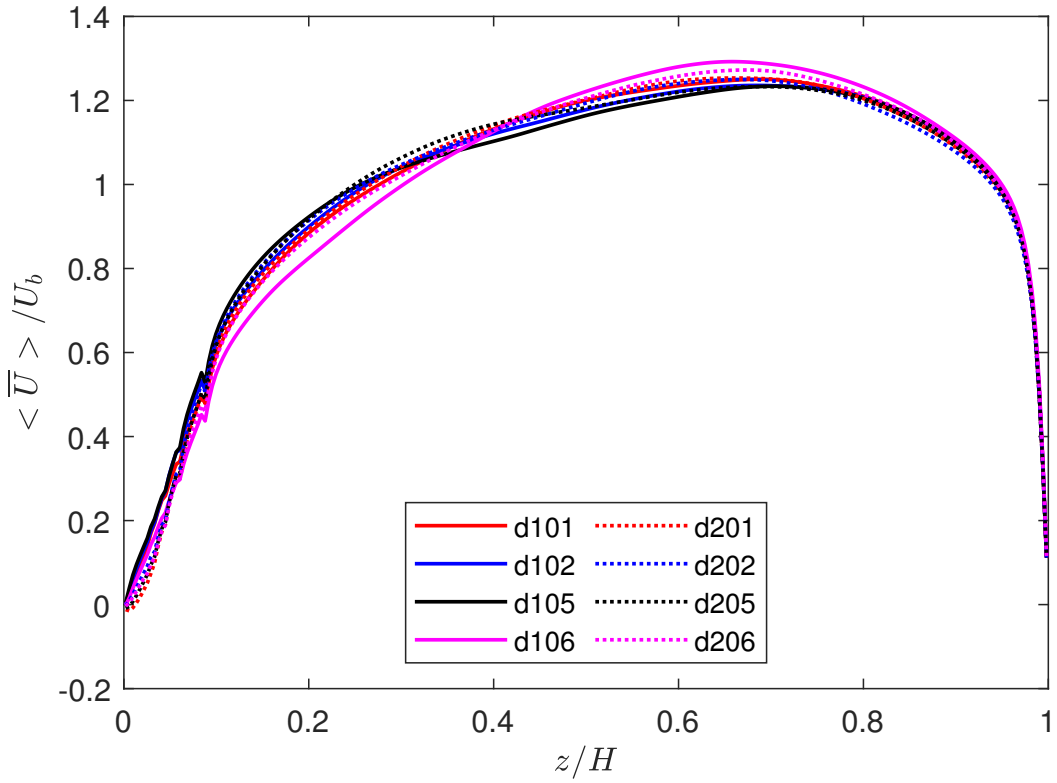

Figure 4.3: Velocity profiles normalized by bulk velocity of the domain for few cases of the two fractal dimensions.

wall effects on the flow. Few kinks are observed near the rough wall side at the height of different generations of cuboids, which can be attributed to a combination of the cubic geometry used in the study and the spatial averaging technique mentioned in equation 4.9.

For fully rough regime atmospheric flows, the velocity field follows a log law profile given as below:

$$U^+ = \frac{1}{\kappa} ln\Big(\frac{z-d}{z_0}\Big) \tag{4.13}$$

Physically, z_0 represents the effective height at which $U(z) = 0$ while d is interpreted as the elevation at which the mean surface drag acts. In terms of the roughness surface, z_0 also represents the momentum deficit or its associated aerodynamic drag while the displacement height (d) modifies the slope of the logarithmic linear ($U(z)$) profile for it to have a collapse in that region. Various methods can be employed in order to compute the displacement height (d) as mentioned in Cheng and Castro [20] i.e by computing the moment of the drag force of individual elements and evaluating the elevation at which moment acts or by using a best fit algorithm to match the slope of the log layer. In the current analysis, evaluation of d based on the best fit algorithm proposed in Zhu *et al.* [12] which then also enables the computation of the roughness length (z_0). In this method, the vertical gradient of Eq. 4.13 is computed and in doing so, z_0 being a constant vanishes and the gradient can be rearranged to obtain the slope equation,

$$\gamma = \frac{z-d}{u_\tau}\frac{dU}{dz} = \frac{1}{\kappa} \tag{4.14}$$

where U is time and spatially averaged velocity.

An iterative process was run by varying the value of d to obtain a best-fit in the inertial layer logarithmic profile, since each d yields a unique $\gamma = \kappa^{-1}$. The value of displacement height maintained was $d \leq 0.75h_1$ (h_1 : height of largest generation cube) during the iteration as a value $d > h_1$ is not physical [40]. Each successive value of d yielded a cumulative error against the logarithmic profile and the value associated with the smallest error was selected. The logarithmic fitting was conducted between heights $z = 1.5h_1$ and $2.5h_1$ in accordance with Yang and Meneveau [4] whose geometry is similar to the current analysis. The corresponding ordinate value from the best-fit yields the value of the roughness length (z_0) of the surface. The von Karman constant is taken to be $\kappa = 0.4$.

Figure 4.5 shows the velocity defect profiles for the rough surfaces against their smooth wall counterparts. The smooth wall velocity profile is plotted in the half channel (H_s) from the top wall until the maximum velocity location for every case and normalized in wall units. It shows a good collapse with the log law for the smooth wall. However, the velocity profiles for both types of fractal surfaces when scaled in wall units do not collapse for the same fractal dimension as seen in 4.5a & 4.5b. This may be due to the in-homogeneity in the distribution of the cuboids for each fractal dimension which is indicative of varying aerodynamic effects on the rough surfaces producing varying roughness lengths and in turn different drag forces. However when scaled with their respective roughness lengths, the velocity profiles show a good collapse in the log region depicting universality as seen in figure 4.6. In figure 4.6, the velocity profiles seem to deviate towards the outer layer showing that z_0 is not a representative scale for the outer layer normalization.

The roughness lengths and the displacement height of the 16 cases studied here are compiled in table 4.1 and the values normalized by h_{rms} are plotted in figure 4.4. The roughness length estimations for the $D = 1$ on an average is higher than that of $D = 2$ with some overlap between the two types of surfaces. This is despite $D = 1$ having lesser number of cuboids (44) and thereby a larger surface area as against $D = 2$ surface (69-73). This is because of a tighter packing of cuboids on the bottom surface for $D = 2$ which creates sheltering and thereby an overall lower drag for the surface. As mentioned in Jiménez [11], roughness flows can be divided into two regimes: the sparse one ($\lambda_f \approx 0.15$) for which roughness length increases with solidity and the dense regime for higher values of λ_f where the roughness effect decreases due to sheltering. As mentioned earlier, the geometric solidity for $D = 1$ is $\lambda_f \approx 0.15$ and for $D = 2$ is $\lambda_f \approx 0.22$ and hence we can expect the value of the drag force to decrease as the fractal dimension increases. This effect will be seen again in the calculation of the skin friction coefficients and heat transfer co-efficients in figure 4.9 & 4.10a.

The average value of the roughness lengths are $z_0/h_{rms} = 0.17$ and $z_0/h_{rms} = 0.13$ for $D = 1$ & $D = 2$, respectively with a corresponding standard deviations of $\sigma_{d=1} = 0.028$ and $\sigma_{d=2} = 0.025$. The values of the roughness lengths as normalized with h_{rms} of the fractal surface falls in the range of $0.1 - 0.2$ which is within the limits mentioned by Zhu *et al.* [12].

4.2. Performance evaluation for rough surfaces

4.2.1. Mean Temperature Profile

The vertical mean temperature profiles across the entire channel height for few cases of the two types of fractal surfaces are presented in figure 4.7. The temperature profile is spatially and temporally averaged as discussed earlier. The temperature profile is normalized with respect to the difference in the wall temperatures ($\Delta T_w = T_h - T_c$, Here T_h is the hot rough wall & T_c is the cold smooth wall) and the vertical distance is normalized by the channel height, H. It can be seen from the figure that the profiles agree well near the smooth upper wall and in the interior of the channel. The flow temperature is very well mixed in the interior. The main difference can be seen near the rough wall sides for the two types of surfaces, where the spatially averaged temperature $< \overline{T} >$ is slightly higher for $D = 2$ cases. In order, to gain a quantitative measure of the increase in heat transfer for the two types of surfaces, the global temperature of the flow ($T_G = \int_0^H < \overline{T} > dz$) in accordance with [41] was plotted in figure 4.8. The global flow temperature of $D = 2$ is slightly higher than for $D = 1$ for all the cases simulated. Few kinks are observed near the rough wall in figure 4.7 which is mainly due to a combination of

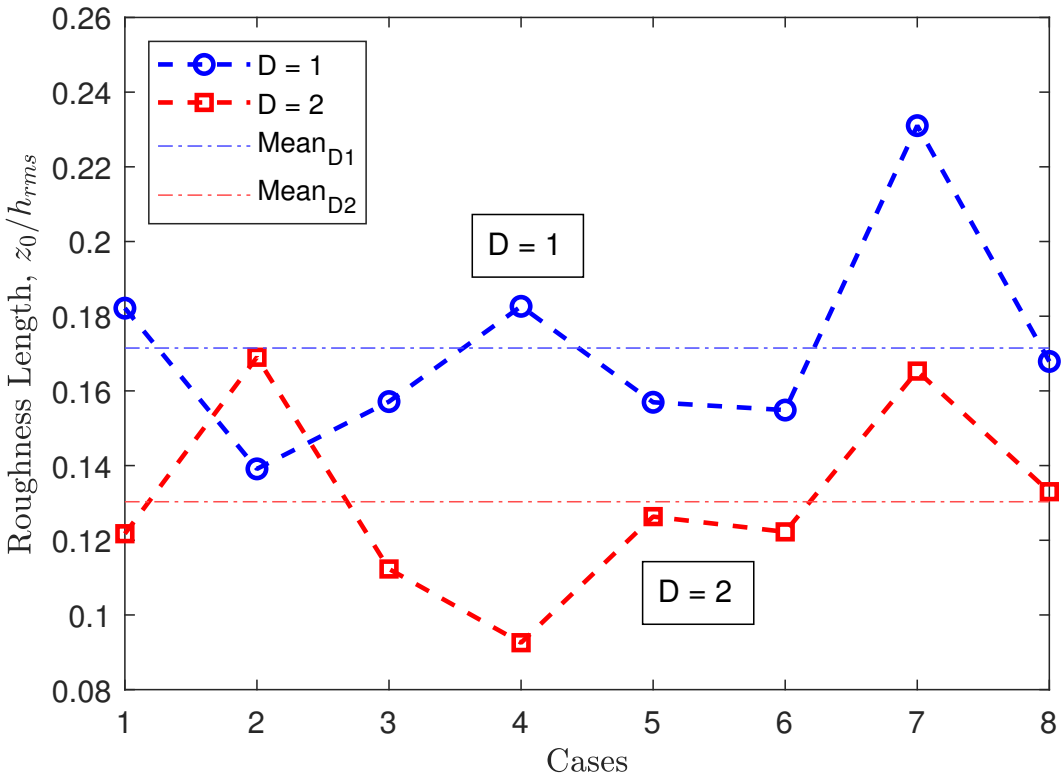

Figure 4.4: Roughness lengths normalized by h_{rms}. Note the h_{rms} values for the two types of roughness are different due to a variation in the total number of cuboids and packing density for the fractal surfaces. Average value of the roughness lengths are $z_0/h_{rms} = 0.17$ and $z_0/h_{rms} = 0.13$ for $D = 1$ & $D = 2$, respectively with a corresponding standard deviations of $\sigma_{d=1} = 0.028$ and $\sigma_{d=2} = 0.025$

.

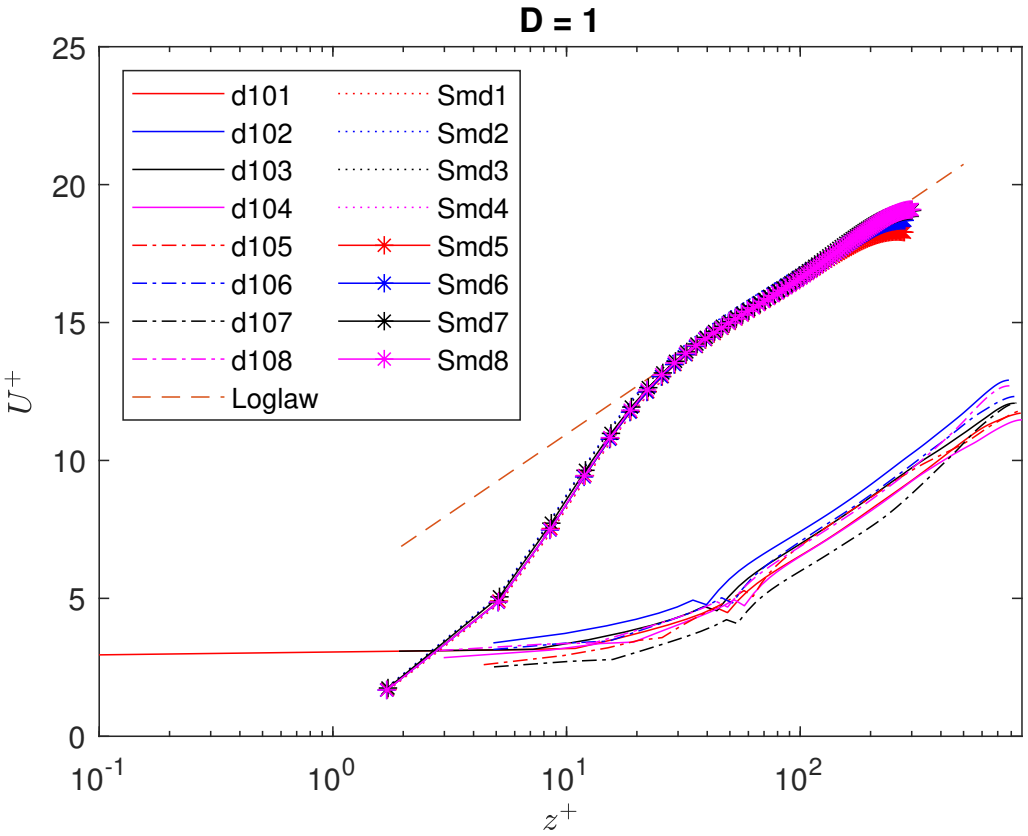

(a) Profile for $D = 1$

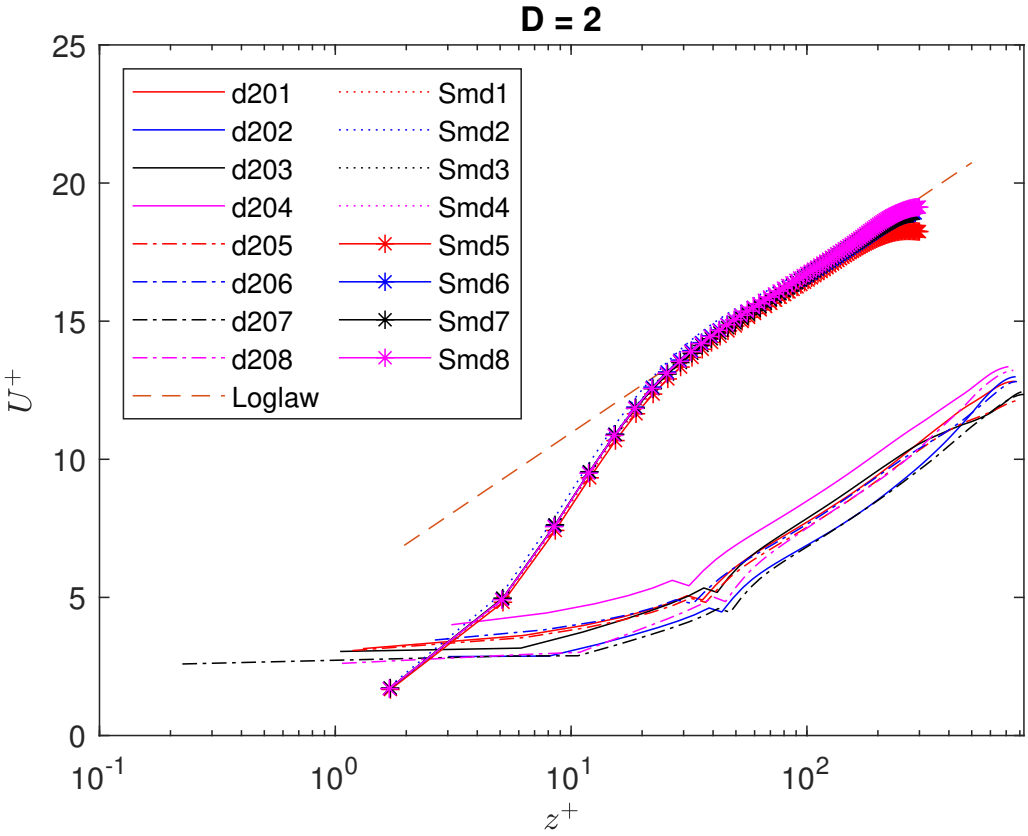

(b) Profile for $D = 2$

Figure 4.5: Plots of velocity normalized by friction scales on two surfaces $D = 1$ & $D = 2$. The x axis scales in adjusted for the displacement height for the rough walls.

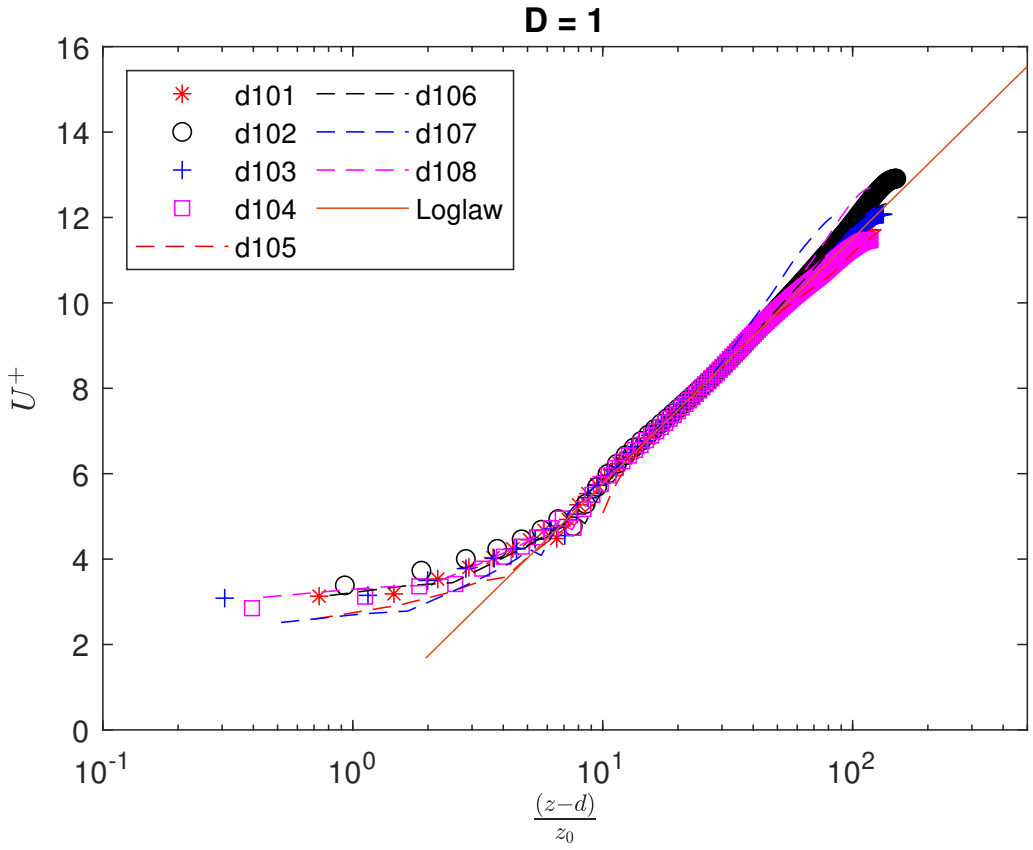

(a) Profile for $D = 1$

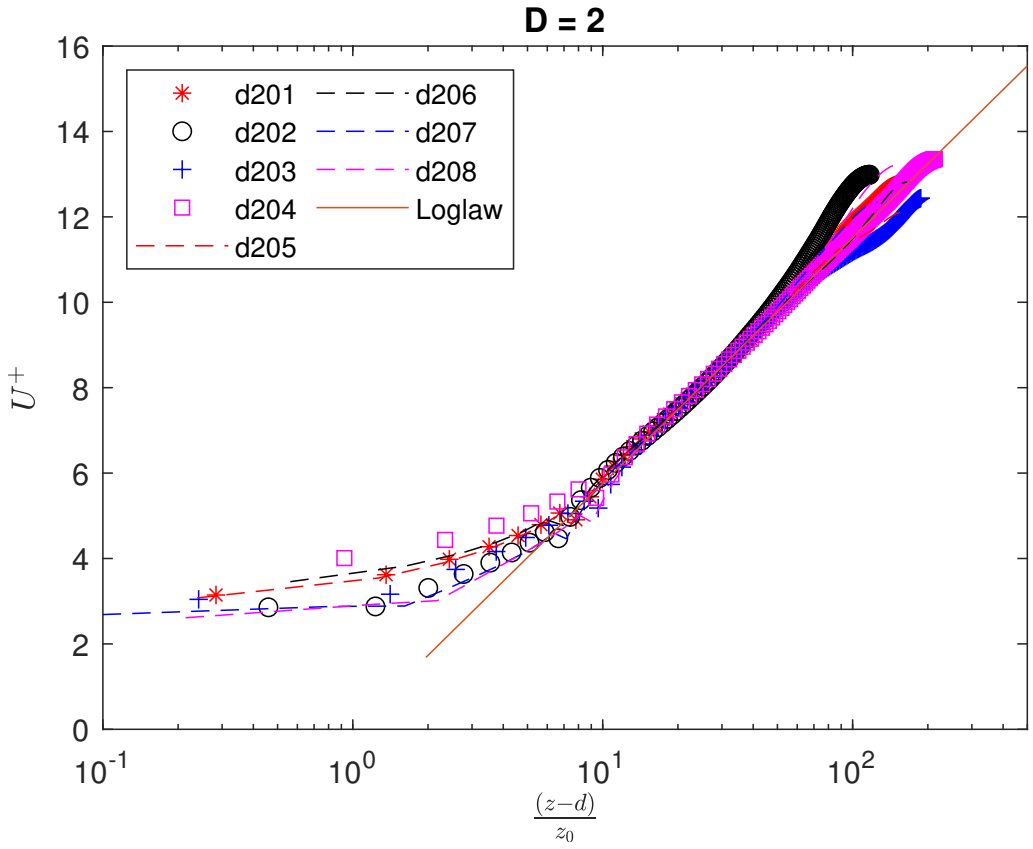

(b) Profile for $D = 2$

Figure 4.6: Plots of velocity normalized by roughness lengths on two surfaces $D = 1$ & $D = 2$. The x axis scales in adjusted for the displacement height for the rough walls.

Table 4.1: Summary of roughness lengths and displacement heights. (h_1: height of the largest generation, h_{rms}: root mean square height of rough surface. Average values of viscous length scales at rough walls are $\delta_{v,d=1} = 0.00445$ & $\delta_{v,d=2} = 0.00467$

Case	d/h_1	z_0/h_1	z_0/h_{rms}
$d1-01$	0.632	0.0645	0.182
$d1-02$	0.681	0.0492	0.139
$d1-03$	0.663	0.0556	0.157
$d1-04$	0.560	0.0647	0.183
$d1-05$	0.500	0.0556	0.157
$d1-06$	0.589	0.0548	0.155
$d1-07$	0.591	0.0818	0.231
$d1-08$	0.607	0.0594	0.168
$d2-01$	0.714	0.0436	0.122
$d2-02$	0.652	0.0607	0.169
$d2-03$	0.670	0.0401	0.112
$d2-04$	0.743	0.0331	0.093
$d2-05$	0.716	0.0452	0.126
$d2-06$	0.749	0.0438	0.122
$d2-07$	0.631	0.0592	0.165
$d2-08$	0.623	0.0476	0.133

the geometry studied (cuboids of various generations) and the spatial averaging procedure defined in equation 4.9. The kinks are observed near the heights of the five generation of cuboids used in the fractal surface.

4.2.2. Friction and heat transfer coefficients for surfaces

In this section, we evaluate the skin friction and the heat transfer parameters to quantify the performance of the two types of surfaces. All the calculations for the parameters are conducted in accordance with the method described in section 4.1.2. It can be seen from figures 4.9 & 4.10, that the Reynolds numbers vary for the rough and smooth wall half channels with the rough wall counterpart being on the higher side. This is mainly because the half channel height of the rough wall is much higher than that of the smooth wall ($H_r > H_s$) and also the local bulk velocities of the respective half channels are different.

Firstly, the skin friction coefficient evaluated as per equation 4.7 for the 16 cases with respect to their bulk Reynolds number is plotted in figure 4.9. The friction coefficients for the smooth wall half channel (H_s) collapse very well with Dean's 1978 correlation ($C_f = 0.073 Re_{bulk}^{-0.25}$). In the calculation of the performance factor, the friction factor for the rough wall is normalized with the corresponding smooth wall value at their corresponding bulk Reynolds number as obtained from Dean's correlation. The friction coefficient for the fractal surface $D = 1$ on an average is higher than $D = 2$ which is expected as mentioned in the previous section due to a higher packing density of the cuboids in $D = 2$ resulting in skimming of the flow over these cuboids. However, there is an overlap in the friction coefficients for the two surfaces as also seen for z_0 values for some realizations.

Now, in order to evaluate the heat transfer performance of the surface we calculate and plot the Nusselt number from equation 4.7 for the 16 cases as shown in figure 4.10a. The half channel Reynolds number used here is based on the 'equivalent' hydraulic diameter which is four times the effective channel height as per equation 4.8. In the current simulations, inflow/outflow conditions for temperature and periodic for velocity are used instead of periodic conditions for both temperature and velocity as in Forooghi *et al.* [36]. Hence, even though the flow is fully developed in terms of momentum but it cannot be considered to be thermally developed due to which the heat transfer coefficients (Nu, St & RA) can increase by a factor of 2-2.5 times the fully developed value Mills [42]. Phillips [43] suggested a factor (ϕ), which incorporates the above effect, and can be used to multiply the fully developed correlation

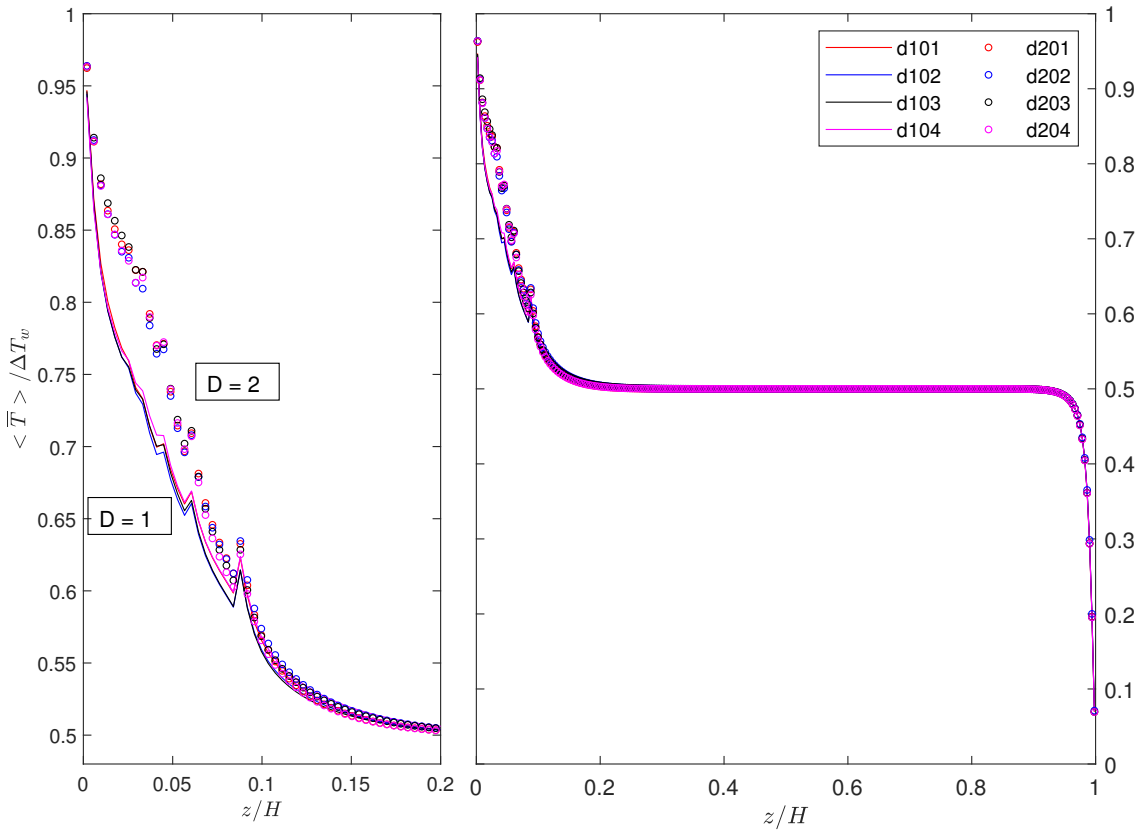

Figure 4.7: Spatially and temporally averaged vertical temperature profiles for few fractal cases of each dimension. Normalization done with $\Delta T_w = T_h - T_c$ where T_h : temperature of hot rough wall & T_c : temperature of cold smooth wall

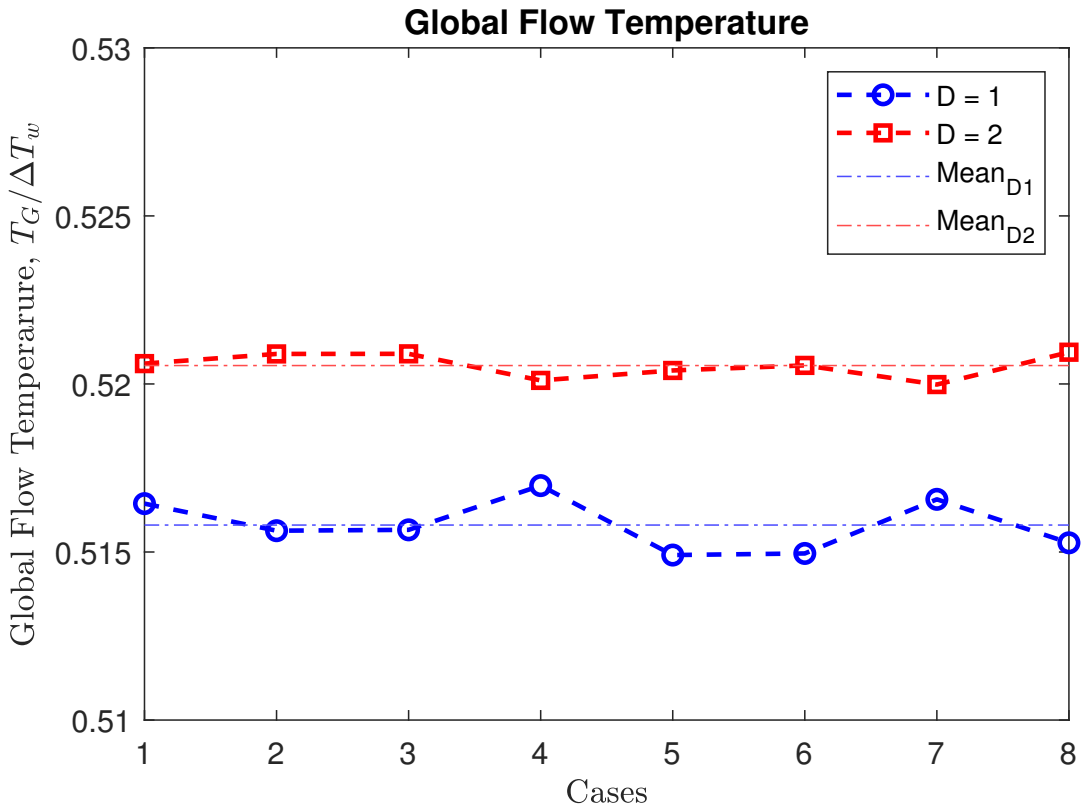

Figure 4.8: Global flow temperature for all cases of the two fractal dimensions. Normalization done with $\Delta T_w = T_h - T_c$ where T_h : temperature of hot rough wall & T_c : temperature of cold smooth wall

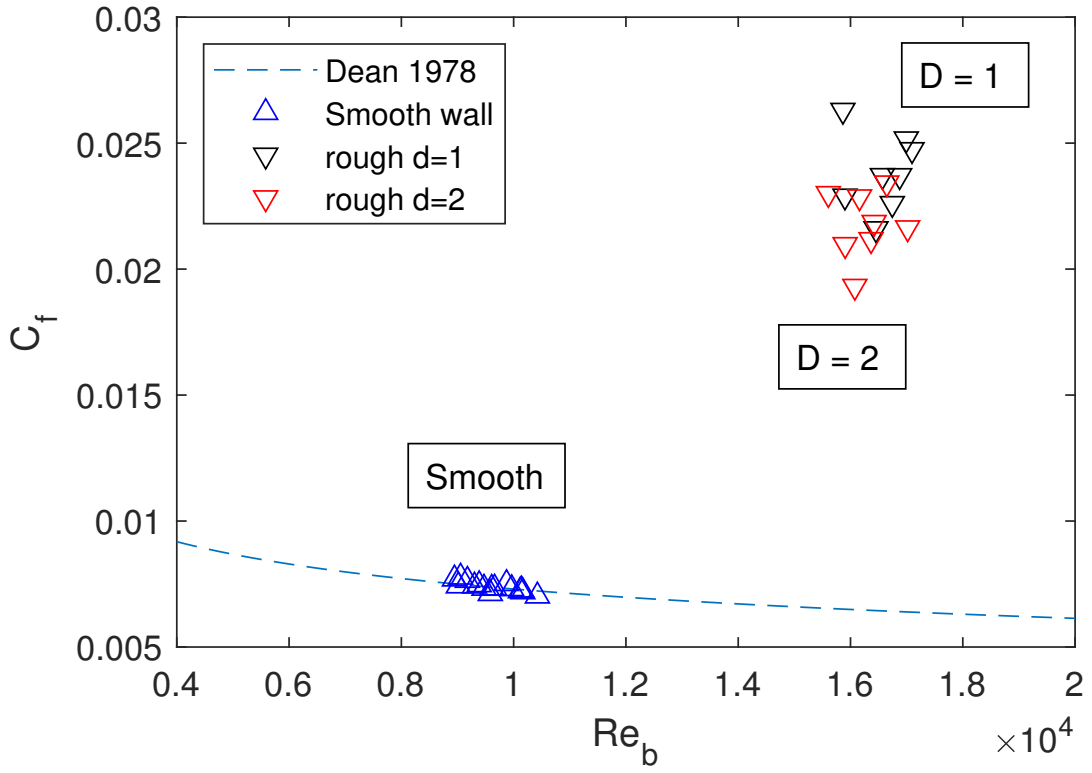

Figure 4.9: Variation of friction coefficient, c_f with bulk Reynolds number for both smooth and rough walls. Dashed line indicated the (Dean 1978) correlation for smooth wall.

to find the corresponding smooth wall values for the current cases. The factor is as below:

$$\phi = 1 + (\frac{D_e}{L})^{\frac{2}{3}} \tag{4.15}$$

where, D_e is the equivalent Diameter of the smooth channel and L is the length of the channel. Three commonly used correlations for Nusselt Number in a fully developed turbulent region for smooth circular ducts/channel flows are mentioned below.

$$\text{Kays \& Crawford, 1993 [44]:} \quad Nu = 0.021\phi Re_{dh}^{0.8} Pr^{0.5} \tag{4.16}$$

$$\text{Dittus \& Boelter, 1985 [45]:} \quad Nu = 0.023\phi Re_{dh}^{0.8} Pr^{0.4} \tag{4.17}$$

$$\text{Philips, 1976 [43]:} \quad Nu = 0.012\phi (Re_{dh}^{0.87} - 280) Pr^{0.4} \tag{4.18}$$

The correlation by Dittus & Boelter, 1985 gives the best fit for the smooth wall values as seen from figure 4.10a and therefore the same is used to estimate the smooth wall Nusselt number at the corresponding rough wall Reynolds numbers for normalization.

A peculiar aspect of this plot is that there is almost a complete overlap in the Nusselt numbers for the two types of surfaces unlike the friction factor plot. This indicates that the fractal dimension $D = 2$ does not significantly improve the heat transfer as compared to $D = 1$ despite having a larger roughness

surface area. This can again be attributed to the higher packing density of the cuboids in $D = 2$ than in $D = 1$ which could result in larger re-circulation zones amidst the cuboids. These re-circulation zones act as thermal barriers [3] and thus, despite having a larger surface area for heat transfer, the heat transfer performance is not significantly improved. It is also observed from figure 4.10a, that the Nusselt number on the rough wall is nearly proportional to Reynolds number and grows with a higher slope compared to that on the smooth wall.

Plots for Stanton number reveal a similar story (figure 4.10b), where almost a complete overlap for $D = 1$ and $D = 2$ surfaces can be seen however a sharp rise with respect to Reynolds number is not seen which may be due to the presence of a fully rough regime. Similar to the Nusselt number, the Stanton number too is evaluated for the smooth wall at relevant reynolds number for the corresponding rough wall cases ($St = \frac{Nu}{Re_{dh}Pr}$).

4.2.3. Performance factors

From the previous section it was seen that the performance $D = 1$ surface is almost similar to $D = 2$ in terms of heat transfer coefficients whereas the skin friction for $D = 1$ was higher than $D = 2$. Therefore, it can be expected that the overall performance of $D = 2$ will be better than $D = 1$ for heat transfer relative to the pressure drop. Further, in this section the performance parameter (PF) will be quantified based on equation 4.10. Also, the relative enhancement (E) of the convective heat transfer (equation 4.12) will be calculated independently.

The Enhancement factor, (E) is plotted for the two kind of surfaces in figure 4.11. The average values of the enhancement factor are $E_{D=1} = 1.45$ & $E_{D=2} = 1.47$ with respective standard deviations of $\sigma_{D=1} = 0.046$ and $\sigma_{D=2} = 0.047$. Hence, it can be seen that even though there is slight increase in the heat enhancement factor, the increment is insignificant and the two fractal dimensions perform similarly based on this parameter. The performance factor, (η_a) and the Reynolds analogy factor (RA/RA_0) are also plotted for the two kinds of surfaces in figure 4.12a & 4.12b. The surface $D = 2$ on an average shows a better enhancement for the performance factors than $D = 1$ because the skin friction induced by $D = 2$ is smaller than $D = 1$ with its heat transfer performance being similar. The mean values of the performance factor are $\eta_{a,D=1} = 1.58$ and $\eta_{a,D=2} = 1.64$ with their respective standard deviations of $\sigma_{D=1} = 0.018$ and $\sigma_{D=2} = 0.035$ while that of the Reynolds analogy factor are $(RA/RA_0)_{D=1} = 0.66$ and $(RA/RA_0)_{D=2} = 0.73$ with respective standard deviations of $\sigma_{D=1} = 0.032$ and $\sigma_{D=2} = 0.043$. The mean values of the Performance factors (η_a & RA/RA_0) as seen from figures 4.12a & 4.12b shows a slightly higher value for $D = 2$. However, on analyzing the uncertainty intervals based on the standard deviation table 4.2 it can be seen that there is a significant overlap between the limits for $D = 1$ and that of $D = 2$ surface. Therefore with the current data, it cannot be concluded that the fractal dimension of the surface significantly impacts the performance factors and more data points are needed for the same.

Table 4.2: Summary of Performance factors for fractal surfaces along with their mean and standard deviations.

Parameter	**Mean**	**Standard deviation,** (σ)	**Uncertainty interval,** $(Mean \pm 3\sigma)$
$E_{D=1}$	1.45	0.046	[1.31 - 1.58]
$E_{D=2}$	1.47	0.047	[1.32 - 1.61]
$\eta_{a,D=1}$	1.58	0.018	[1.53 - 1.64]
$\eta_{a,D=2}$	1.65	0.035	[1.54 - 1.75]
$(RA/RA_0)_{D=1}$	0.66	0.033	[0.56 - 0.76]
$(RA/RA_0)_{D=2}$	0.73	0.043	[0.6 - 0.85]

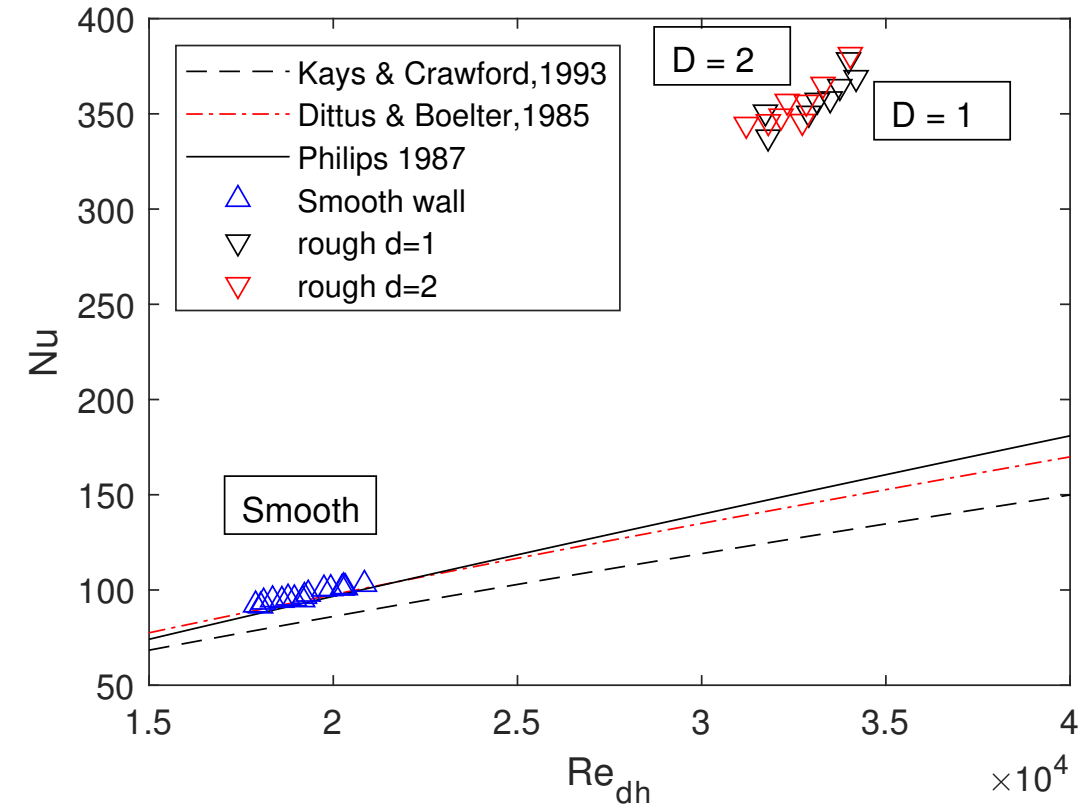

(a) Nu vs Re_{dh}

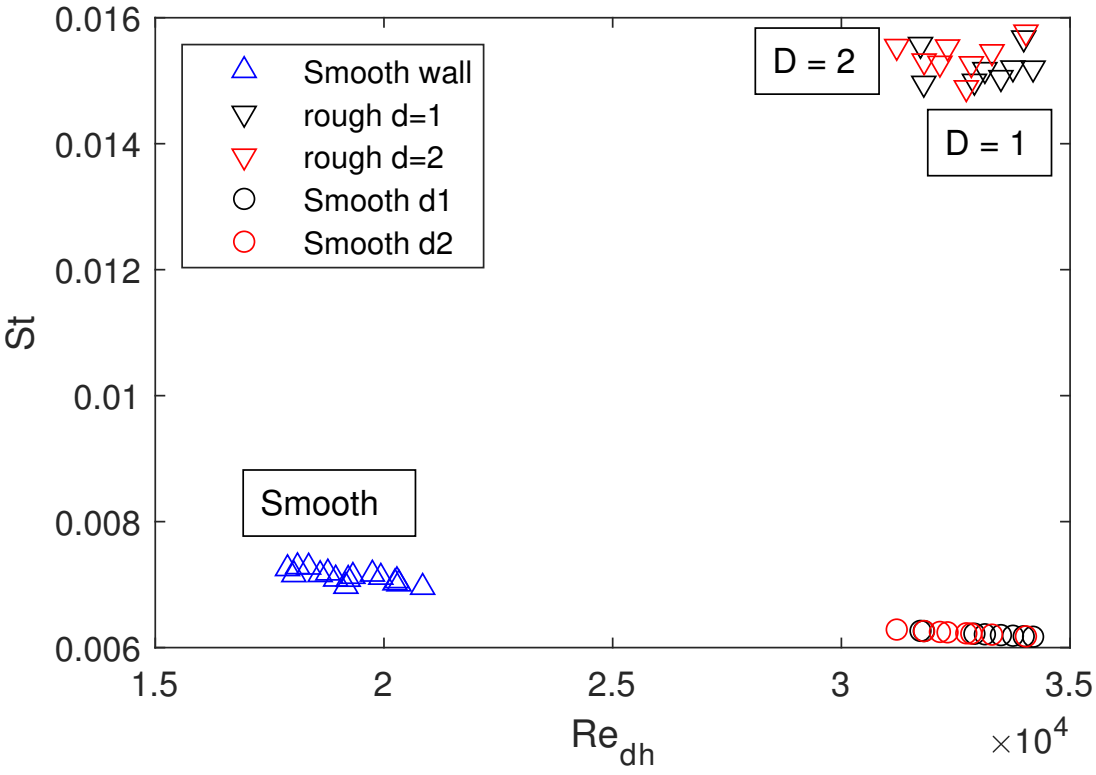

(b) St vs Re_{dh}

Figure 4.10: (a) $Nu\ vs\ Re_{dh}$ (b) $St\ vs\ Re_dh$. Here the hydraulic Reynolds number Re_{dh} for both smooth and rough walls is used. Dashed line indicates the (Kays & Krawford, 1993) and (Dittus & Boelter, 1985) correlation for smooth wall as defined in eq. 4.16, 4.17 & 4.18. The symbols Sm_{d1} & Sm_{d2} indicate smooth wall Stanton numbers at corresponding rough wall values Reynolds number.

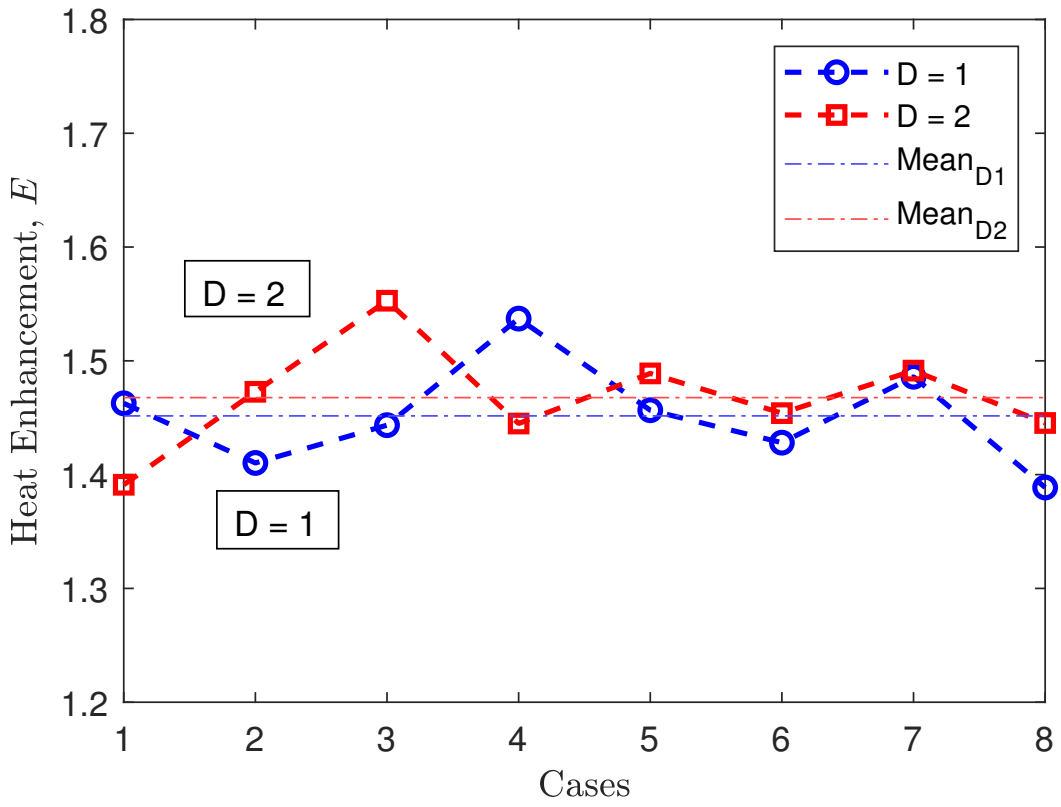

Figure 4.11: A representation of heat transfer enhancement factor (E) & for the two types of surfaces. The dotted line represents the mean value for a particular fractal dimension. The mean values of the enhancement factor are $E_{D=1} = 1.45$ & $E_{D=2} = 1.47$ with respective standard deviations of $\sigma_{D=1} = 0.046$ and $\sigma_{D=2} = 0.047$

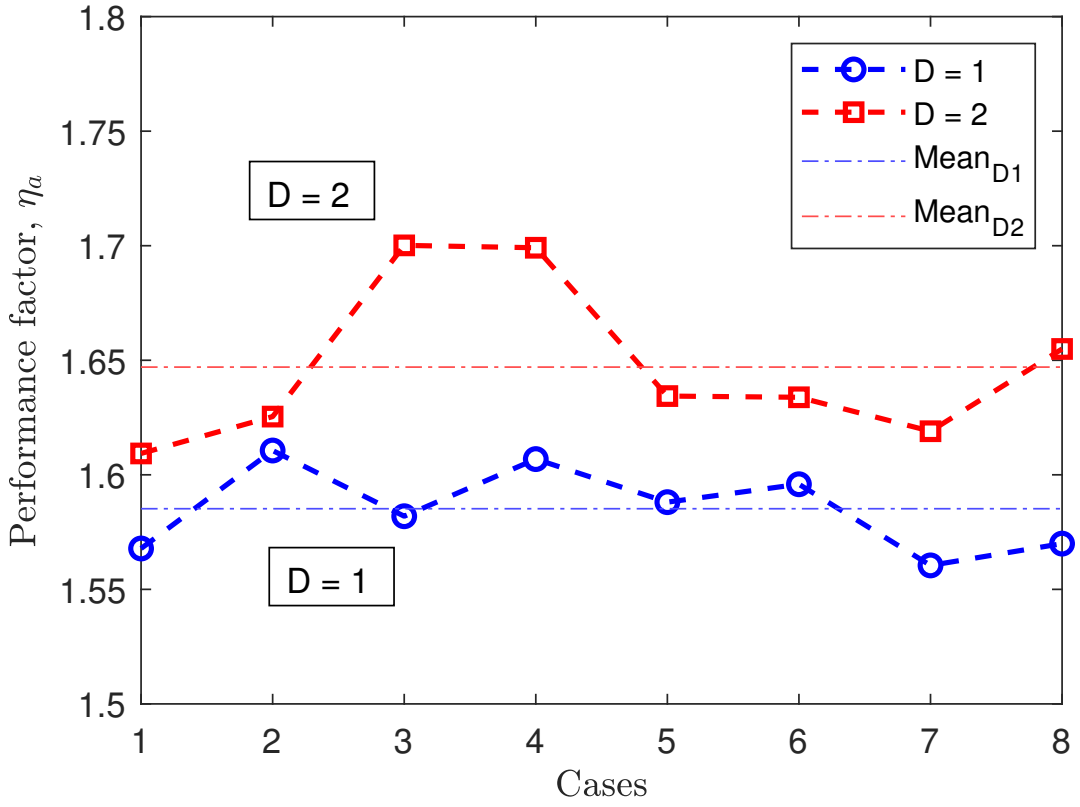

(a) Performance factor, η_a

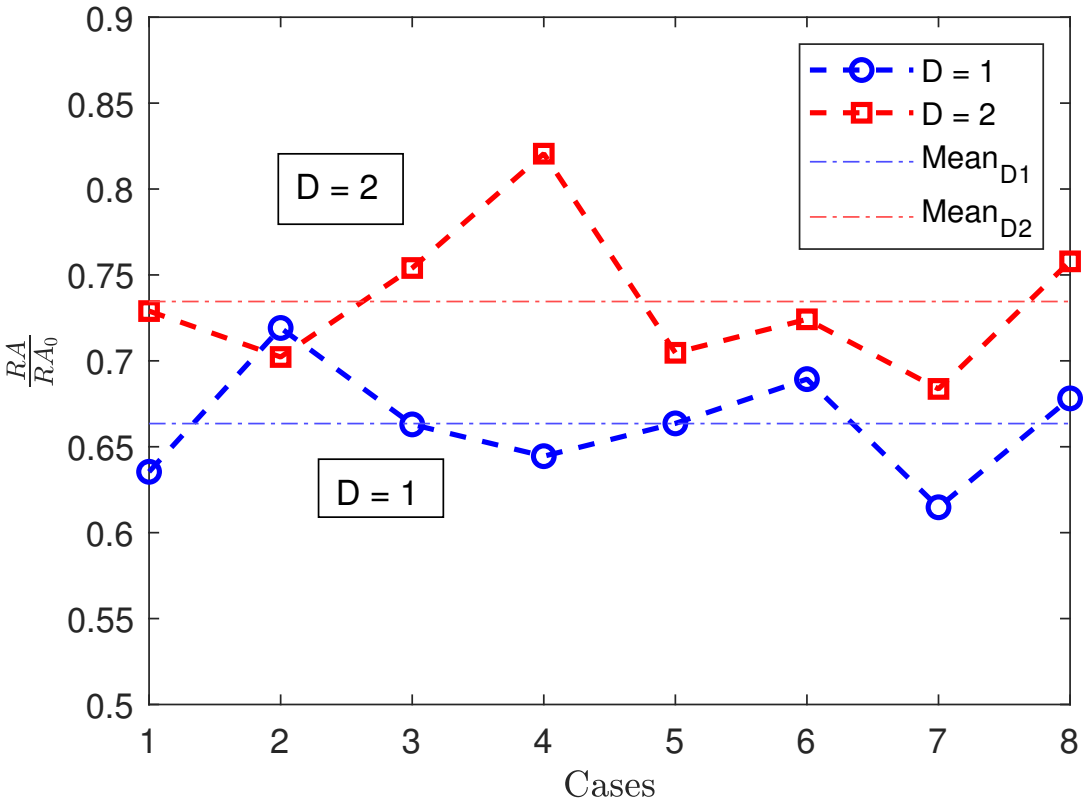

(b) RA/RA_0

Figure 4.12: A representation of performance factor (η_a) for the two types of surfaces. The dotted line represents the mean value for a particular fractal dimension. (Mean values for $D = 1$ ($E = 0.51$ & $\eta_a = 0.97$) and $D = 2$ ($E = 0.27$ & $\eta_a = 0.85$)

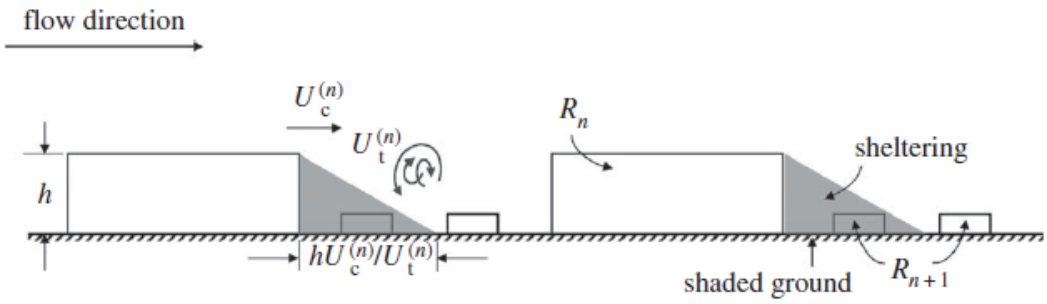

Figure 4.13: A schematic representing flow sheltering that occurs amidst flow over array of cuboids referred from Yang and Meneveau [4]. Here R_n represents the largest scale cuboids whereas R_{n+1} represents the next lower generation. The shaded area is the sheltered region with reduced momentum. U_c is the convective velocity at the top of the roughness elements and u_τ is the velocity scale of turbulent mixing.

4.2.4. Flow Sheltering for rough surfaces

As discussed previously, the roughness length (z_0) for $D = 2$ surface is on an average lower than that of $D = 1$ despite having larger number of cuboids than the latter. This is mainly attributed to the higher packing density of $D = 2$ as compared to $D = 1$ which results in flow sheltering.

Randomly created rough surfaces with the same fractal dimension also have the same solidity. However, large cuboids shelter small ones and the number of exposed cuboids may fluctuate due to the random placement of cuboids. A schematic representation of flow sheltering occurring in flow over an array of cuboids is shown in figure 4.13 [4]. As can be seen from figure 4.13, the larger generation cuboids create a shelter zone (low momentum zone) which shields the smaller generation cuboids that are directly within that zone (grey area indicated in the figure). This phenomenon results in a lesser drag for the rough surface even though the cuboids on this surface are densely packed.

In chapter 2, geometric shelter factors were briefly mentioned wherein the length of the shelter zone, L_n (also called fetch) was arbitrarily chosen to be a multiple of the cube height ($L_n = h_1, 2h_1, 4h_1 \& 8h_1$) and the shelter area was predicted by multiplying it with the cuboid width. Based on this area, the cuboids falling in this shelter were neglected in the calculation for solidity thereby introducing a variation in the "sheltered" solidity of different realizations (whose ordinary solidity is a constant determined by the fractal dimension D). However, an analytical estimate could also be made for the sheltering area based on Yang and Meneveau [4] from the computed convective velocity (U_c) above the largest generation of roughness elements and the velocity scale for turbulent mixing (u_τ). Both the above parameters are calculated a posteriori where U_c is the spatially and temporally averaged velocity profile integrated over a height of 0.2 times the maximum cube height above the largest cube generation and u_τ is the friction velocity at the rough wall. From this we can estimate the fetch (L_n) it takes for the low momentum region to be consumed by equating the stream wise travel time (L_n/U_c) to the available transverse displacement time (h_n/u_τ) where h_n is the height of the largest generation of cuboids. Therefore, the fetch can be given as below:

$$L_n \sim \frac{h_n U_c}{u_\tau} \tag{4.19}$$

From above, a preliminary value of the fetch length was computed for $D = 1$ and $D = 2$ which resulted in a mean value of $L_n \approx 6.4h_1$ (or $3.2L$ where L:cuboid width) and $L_n \approx 6.8h_1$ (or $3.4L$). However, in this estimation the fetch length was computed by considering U_c above the largest generation of cuboids which could be higher than the lower generations and thus the fetch of the lower generations could be lower than the above mentioned values. Hence, the actual average fetch length will be lower than the above values. Additionally, time averaged velocity contours over different slices in the $x - z$ plane were compared for $D = 1$ and $D = 2$ surfaces to get an estimate for the shelter length in figure

4.15 & 4.16. The elevation of the domain (z -dir) is limited only to a height of $4h_n$ in order to capture the details better. Figure 4.14 shows a three dimensional view of the slices taken over the cuboids for one realization of both the fractal surfaces.

It can indeed be seen from figure 4.15 & 4.16 that due to the dense packing of the cuboids the re-circulation regions of the windward side cuboids always encounter the leading edge of the cuboids placed behind them before reattaching to the surface. This can be seen from the constant contour lines shown in figures 4.15 & 4.16. However, from the scales marked along the domain edges the contours for zero or negative velocities (representing re-circulation zones) could be estimated as $4 - 4.5h_n$ (The largest generation windward side cube for both $D = 1$ & $D = 2$ could be seen as example). Hence, we will consider a re-circulation zone length of $4h_n$ which equates to a shelter factor of 4 for further analysis.

As discussed earlier, it was of interest to know if the fractal dimension of the surface was a representative parameter and also if the different random realizations studied had any aerodynamic variation in them. Estimation of roughness lengths did indeed enlighten about the variation in different realizations of a fractal surface with an overlap obtained for few realizations as shown in figure 4.4. Another way to distinguish between the surfaces is through the sheltering effect. Therefore, by considering a shelter factor of 4, a plot is made for the performance factors (η_a & RA/RA_0) as a function of the solidity (λ_f) as shown in figure 4.17a. It can be seen that the two performance factors (η_a and RA/RA_0) show a much stronger correlation with the "sheltered solidity" in the fluctuating realizations displaying an increasing trend. The fractal dimension is not a significant parameter in dictating the heat enhancement even though the two surfaces for $D = 1$ and $D = 2$ look very different.

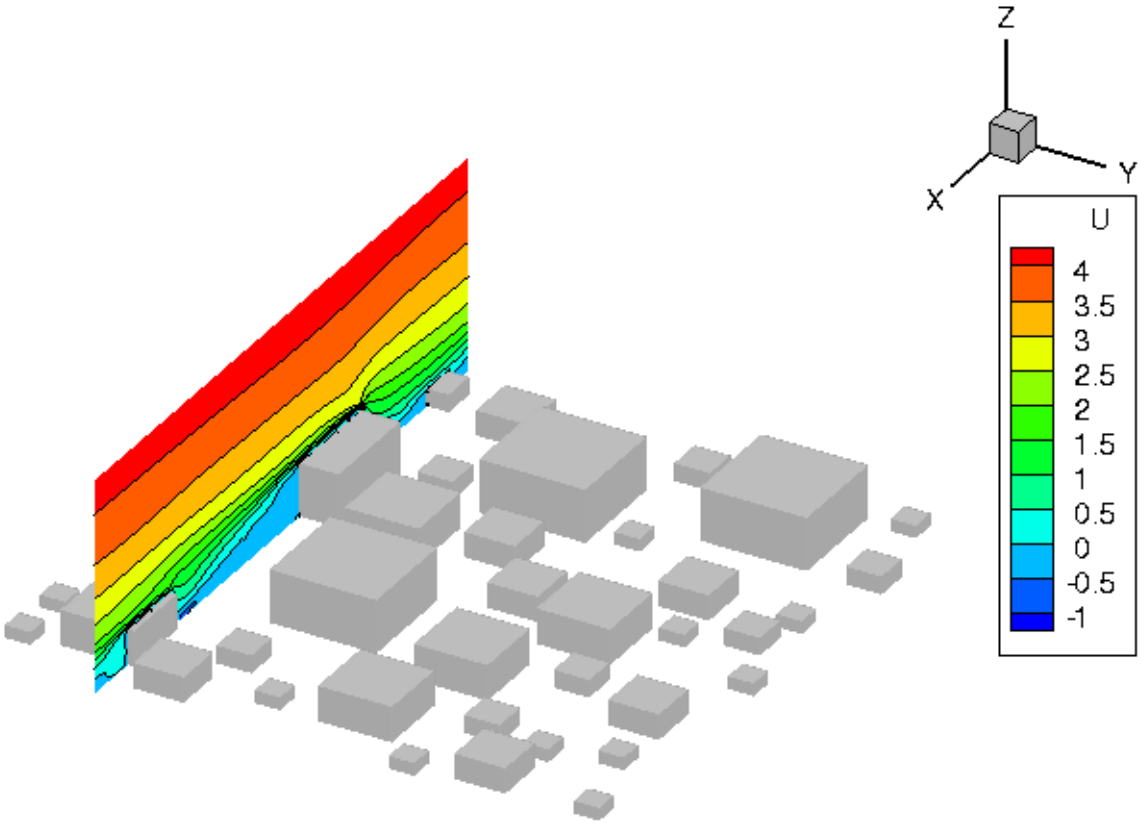

(a) $D = 1$

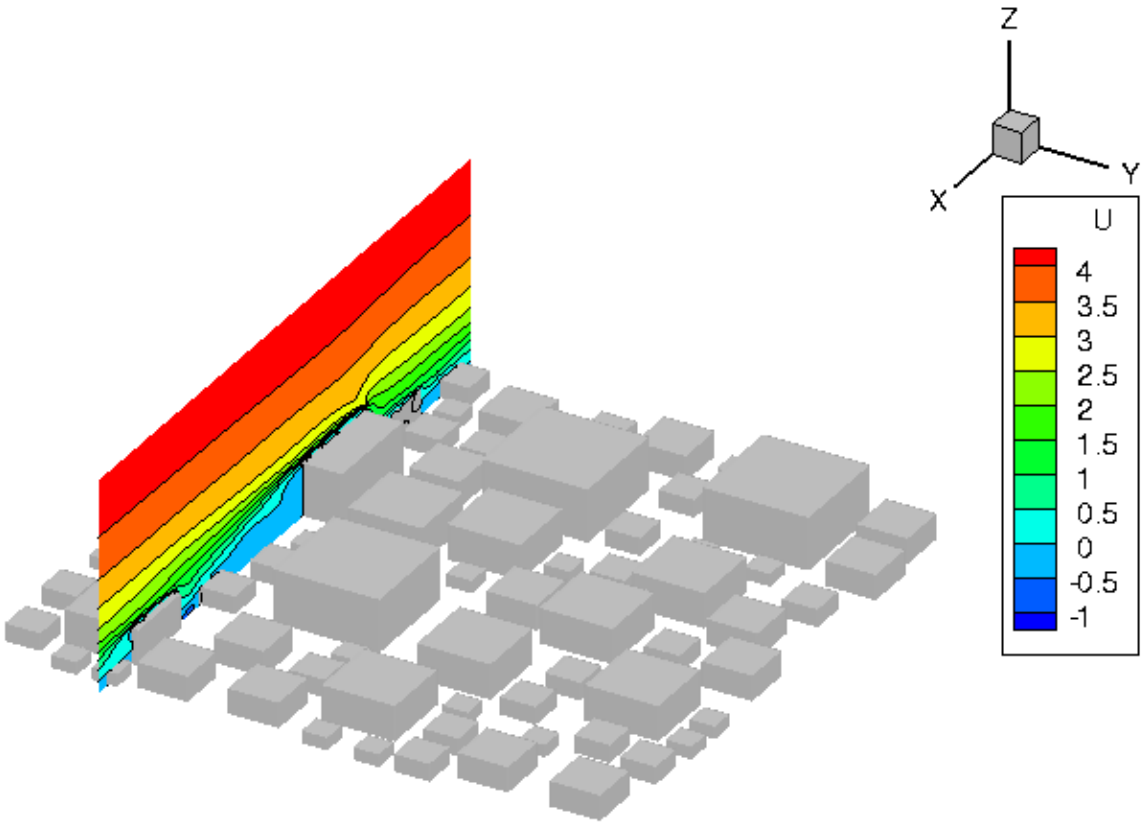

(b) $D = 2$

Figure 4.14: Representation of the slices evaluated to gauge the wake of the cuboids. Three planar (x-z) locations intersecting the larger generation cuboids are selected.

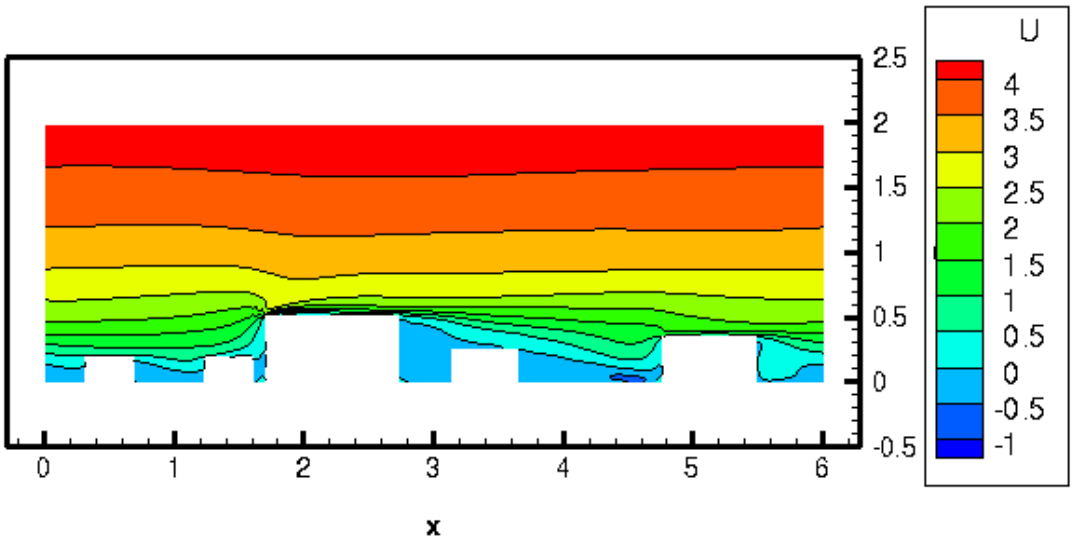

Figure 4.15: Averaged velocity profiles over cuboids to gauge the wake of the cuboids for $D = 1$ (Case $d1 - 01$) at three y locations. The re-circulation zone behind the cuboids tend to extend until a distance of $4 - 4.5h$. The flow direction is from left to right. Contour slices are taken in the x-z plane and the white patches indicate intersection with cuboids.

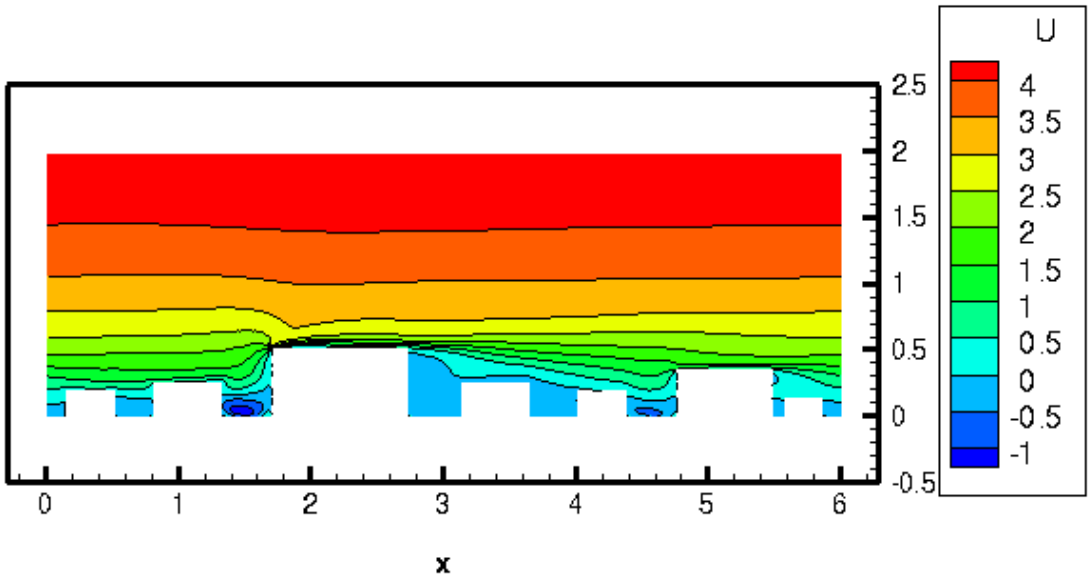

Figure 4.16: Averaged velocity profiles over cuboids to gauge the wake of the cuboids for $D = 2$ (Case $d2 - 01$) at three y locations. The re-circulation zone behind the cuboids tend to extend until a distance of $4 - 4.5h$. The flow direction is from left to right. Contour slices are taken in the x-z plane and the white patches indicate intersection with cuboids.

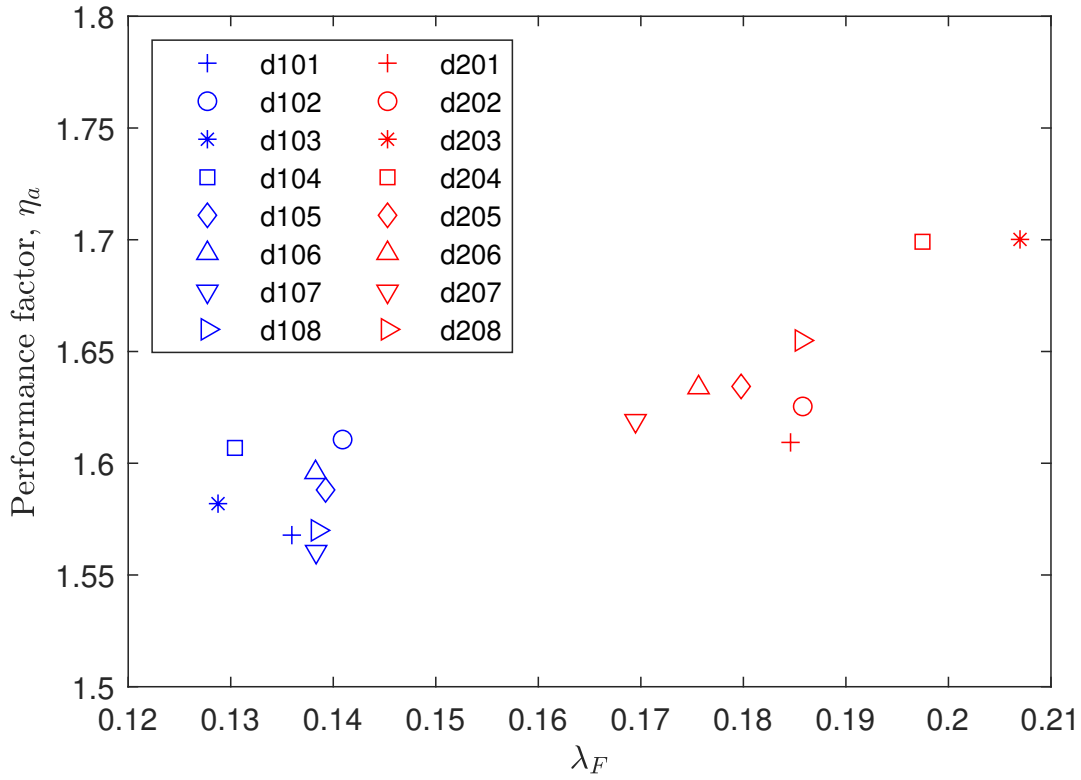

(a) η_a vs λ_f

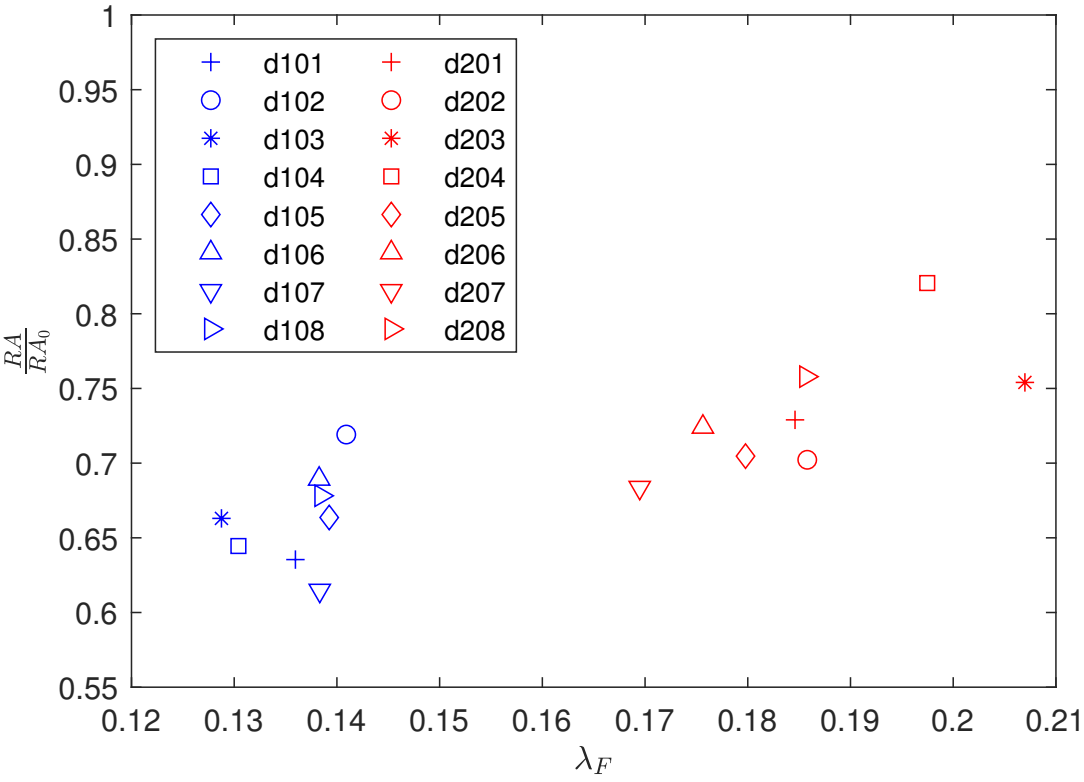

(b) RA/RA_0 vs λ_f

Figure 4.17: (a) η_a vs λ_f (b) RA/RA_0 vs λ_f. Frontal solidity with geometric shelter of 4 for both graphs

5

Conclusion & recommendations

5.1. Conclusion

In this thesis, the role of fractal dimension of a rough surface in the heat transfer performance is studied using DNS. The fractal surfaces are designed by randomly placing several generations of self-similar cuboids with varying size distributions. The quantity of cuboids sprinkled for each generation follows a fractal dimension (chapter 2). Two fractal dimensions i.e. $D = 1$ and $D = 2$ with eight random realizations of each are studied to find the averaged effect of the heat performance factors over the kinds of surfaces. A numerical model is designed to simulate the above (chapter 3) with the cubes being modelled using an immersed boundary method [1] and the domain is made parallel in the x-direction.

Based on the analysis in this thesis, the results can be summarized as below:

1. Roughness lengths for the two types of surfaces were estimated and it was found that the mean value for $D = 1$ was higher than that of $D = 2$. This may be attributed to the higher solidity of $D = 2$ surface which creates more sheltering and thereby an overall lower drag for the surface.
2. The analysis for the performance factors (η_a and RA/RA_0) and the enhancement factor (E) was done for the two types of surfaces. The enhancement factor, E showed an insignificant increase with the fractal dimension. For the case of the performance factors (η_a and RA/RA_0), their mean value was higher for $D = 2$ as compared to $D = 1$. However, based on analysis of the standard deviation of these parameters for different realizations there was a significant overlap in the uncertainty intervals of the two surfaces. Hence, it cannot be conclusively said that increasing the fractal dimension of the surface significantly impacts the heat transfer performance for the current cases.
3. For different realizations of a fractal dimension there is a variation in the number of sheltered cuboids falling within the re-circulation zones of larger generation cuboids due to their random placement. This produces a fluctuation in the ”sheltered” solidity for different realizations within the same fractal dimension. The length of the shelter zones behind the cuboids was estimated to be $4 - 4.5h_n$ (h_n: height of the cuboids, n: generation) which translates to a shelter factor of 4. Plots for performance factors as a function of the ”sheltered” solidity (Shelter factor = 4) were made which showed an increasing trend. The plots also reveal a strong correlation between the ”sheltered” solidity and the heat transfer performance for the fluctuating realizations.

5.2. Recommendations

The present work can be extended with the following recommendations.

1. The current thesis only explore self-similar cuboids of varying sizes, however, as per Forooghi *et al.* [7] it is known that the shapes of roughness structures could also impact the heat transfer performance. Hence, it will be interesting to study other shapes in a similar fractal arrangement.
2. As established in the above thesis, the ”sheltered” solidity (λ_f) of various realizations of the fractal surfaces had a very strong correlation with the performance factors. Hence when selecting different realizations to represent a fractal dimension, realizations with similar ”sheltered” solidity must be chosen.
3. In the current thesis, inflow-outflow boundary conditions were used for temperature in the stream-wise direction which resulted in higher heat fluxes. However, it will be interesting to study the current cases with periodic boundary conditions for temperature in the stream-wise direction which could simulate thermally fully developed flow.

A

Appendix A

A.1. Turbulent flow over a single wall mounted cube

In order to validate the scalar turbulence code, a simple case of turbulent flow over a wall mounted cube is conducted and validation is done with a corresponding simulation in ANSYS FLUENT. The domain geometry used for the setup is as shown in the figure A.1.

The domain size is scaled according to the length of the cube ($\mathcal{D}$). In the streamwise (x), lateral (y) and vertical (z) directions, we have the domain size as $4\mathcal{D}$ x $4\mathcal{D}$ x $3.4\mathcal{D}$ respectively. The grid resolution is (100 x 100 x 80) in the three directions respectively. Grid stretching is used near the cube faces and top and bottom walls with the first grid point being at a distance of $0.01\mathcal{D}$. Periodic boundary conditions are used for velocity and temperature in the stream-wise and lateral directions whereas, a no-slip boundary condition is applied for velocity at the walls in the z-direction. For temperature, the top and bottom walls are maintained at $T_c = 0$ whereas the cube is maintained at a temperature of $T_h = 10$.

The simulations were carried out at a bulk Reynolds number of 13000. First order statistics for the turbulent flows were plotted along the vertical and lateral directions for U, W and T. The velocities in this case are normalized with respect to the bulk velocity in the channel, ($U_b = 3.86$) and the temperature is normalized with respect to the temperature difference between the hot cube and the cold wall, ($T_h - T_c = 10$, where T_h: Cube Temperature and T_c: Wall temperature). Three stream-wise locations are used for plotting the vertical and lateral profiles at distances $x/h = 1.2\mathcal{D}$, $x/h = 1.8\mathcal{D}$ and $x/h = 2.7\mathcal{D}$ (h: channel height, $3.4\mathcal{D}$) which represent location in front of the cube, intersecting the cube and behind the cube respectively. It can be seen from figures A.2, A.3 and A.4 that there is a fair agreement between the two simulations. Certain discrepancies are observed, although it may be attributed to the fact that a constant pressure gradient method was used for forcing periodic conditions in ANSYS whereas a constant mass flow rate method was used in the DNS. Due to this, the mass flow rate in DNS was constant at 52.7 while that in ANSYS fluctuated around 51.36. Moreover, the grid used in ANSYS is a collocated one as against the staggered grid used in the DNS. Similarly, lateral profiles are shown in figures A.5, A.6 and A.7.

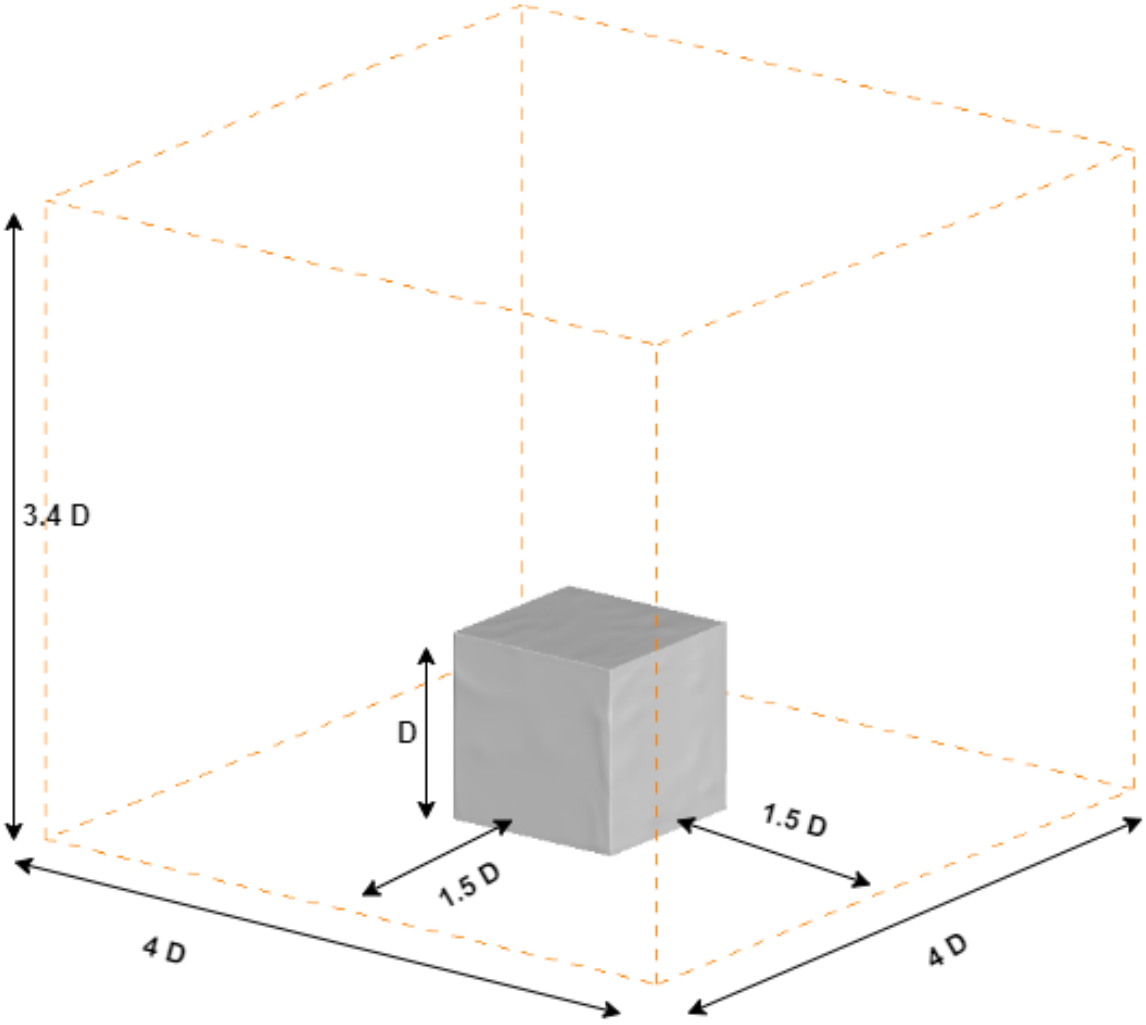

Figure A.1: Domain used for simulating a heat transfer in turbulent flow over a single cube. The origin is considered to be at the bottom left corner.

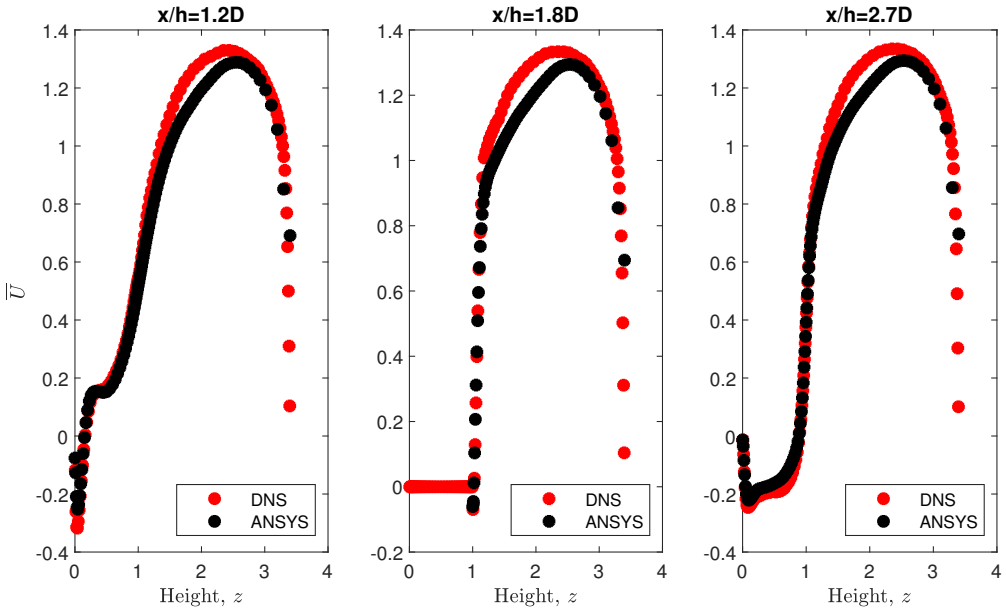

Figure A.2: Time averaged streamwise velocity ($\overline{U}$) along the vertical height at three locations in the mid plane of the domain at $x/D = 1.2$, $x/D = 1.8$ and $x/D = 2.7$. The three locations correspond to x-locations just in front of the cube, on top of the cube and behind the cube. The velocity is normalized by the bulk velocity, $U_b = 3.86$

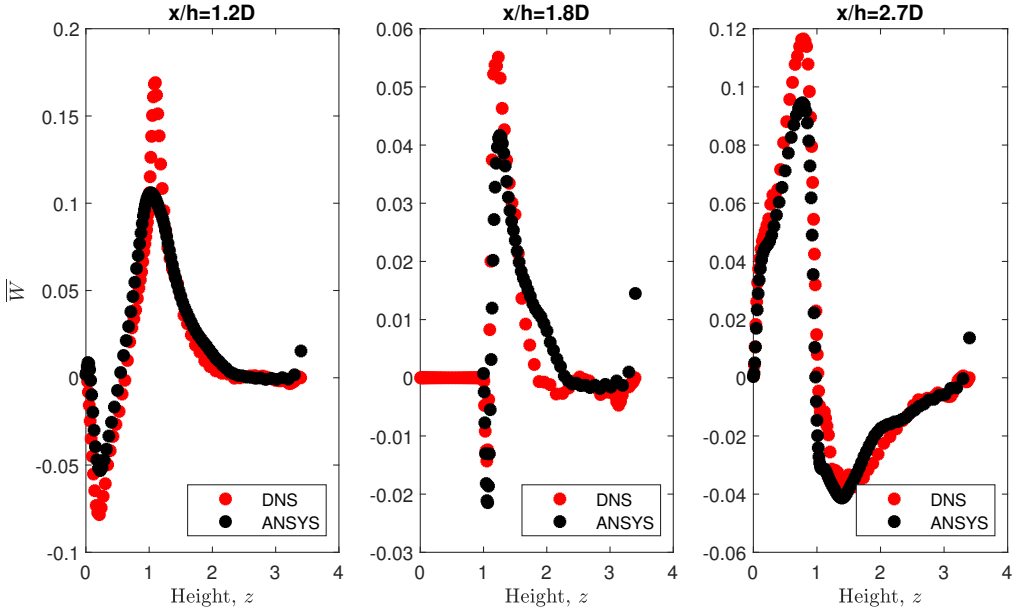

Figure A.3: Time averaged vertical velocity ($\overline{W}$) along the vertical height at three locations in the mid plane of the domain at $x/D = 1.2$, $x/D = 1.8$ and $x/D = 2.7$. The three locations correspond to x-locations just in front of the cube, on top of the cube and behind the cube. The velocity is normalized by the bulk velocity, $U_b = 3.86$

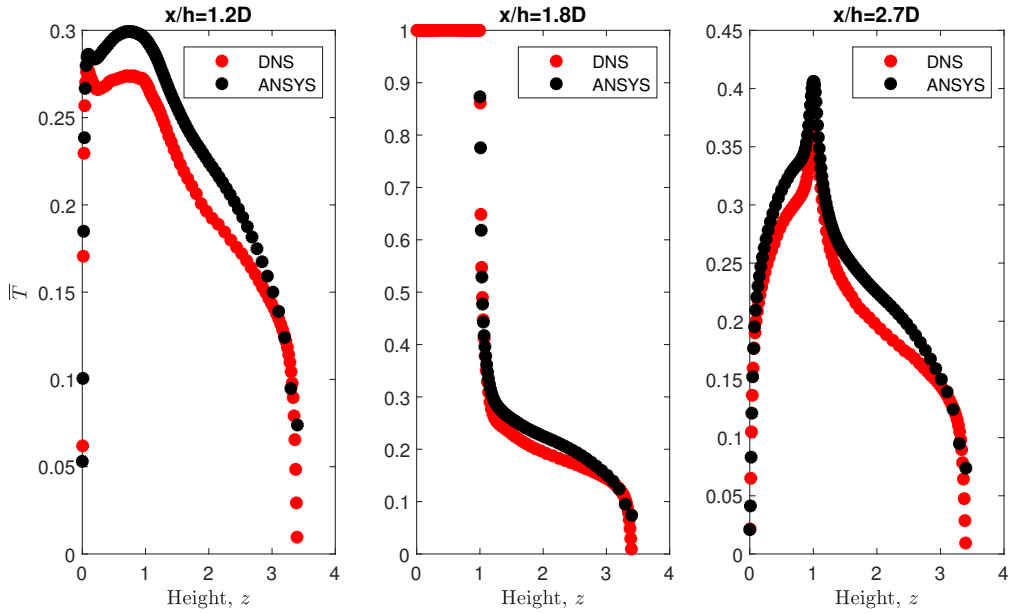

Figure A.4: Time averaged temperature ($\overline{T}$) along the vertical height at three locations in the mid plane of the domain at $x/D = 1.2$, $x/D = 1.8$ and $x/D = 2.7$. The three locations correspond to x-locations just in front of the cube, on top of the cube and behind the cube. Normalization is done by the temperature difference between the hot cube and the cold wall, ($T_h - T_c = 10$, where T_h: Cube Temperature and T_c: Wall temperature)

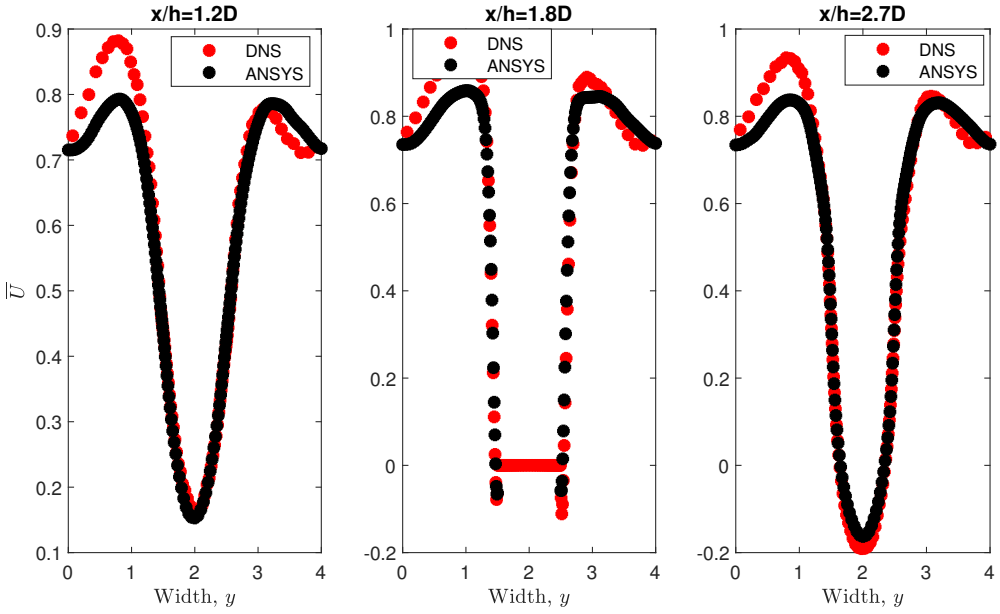

Figure A.5: Time averaged stream-wise velocity ($\overline{U}$) along the lateral width at three stream-wise locations of $x/D = 1.2$, $x/D = 1.8$ and $x/D = 2.7$ and height of $z/D = 0.5$. The three locations correspond to x-locations just in front of the cube, cutting through the cube and behind the cube. The velocity is normalized by the bulk velocity, $U_b = 3.86$

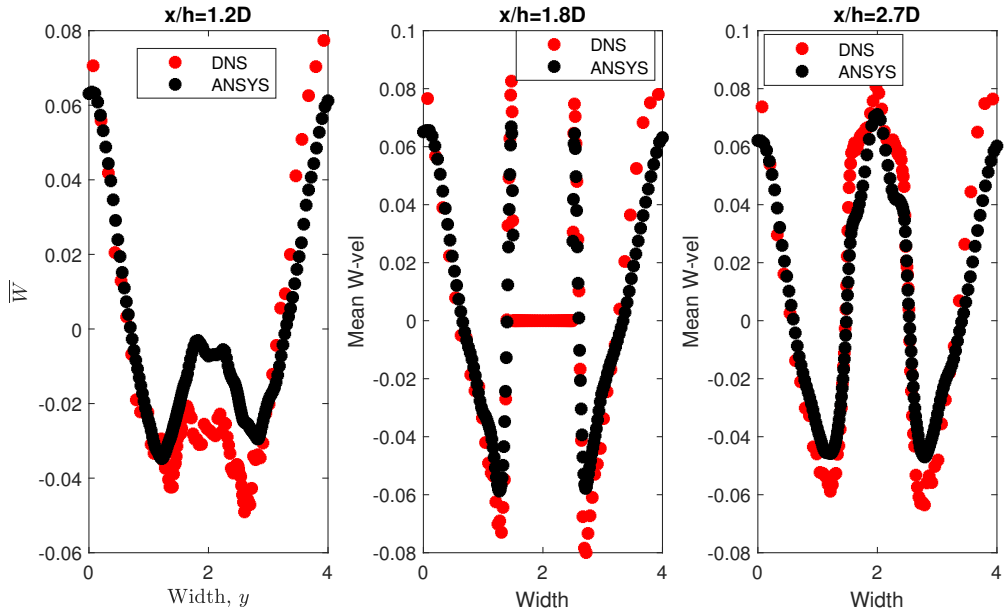

Figure A.6: Time averaged vertical velocity ($\overline{W}$) along the lateral width at three stream-wise locations of $x/D = 1.2$, $x/D = 1.8$ and $x/D = 2.7$ and height of $z/D = 0.5$. The three locations correspond to x-locations just in front of the cube, cutting through the cube and behind the cube. The velocity is normalized by the bulk velocity, $U_b = 3.86$

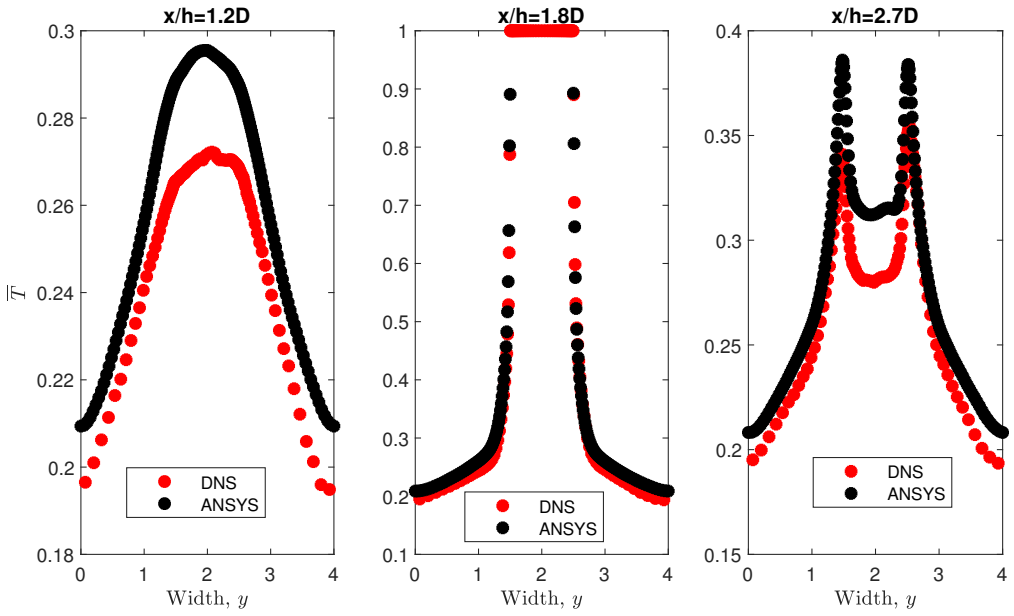

Figure A.7: Time averaged temperature ($\overline{T}$) along the lateral width at three stream-wise locations of $x/D = 1.2$, $x/D = 1.8$ and $x/D = 2.7$ and height of $z/D = 0.5$. The three locations correspond to x-locations just in front of the cube, cutting through the cube and behind the cube. Normalization is done by the temperature difference between the hot cube and the cold wall, ($T_h - T_c = 10$, where T_h: Cube Temperature and T_c: Wall temperature)

Bibliography

[1] M. Pourquie, W.-P. Breugem, and B. J. Boersma, *Some issues related to the use of immersed boundary methods to represent square obstacles,* International Journal for Multiscale Computational Engineering **7** (2009).

[2] O. Reynolds, *Xxix. an experimental investigation of the circumstances which determine whether the motion of water shall be direct or sinuous, and of the law of resistance in parallel channels,* Philosophical Transactions of the Royal society of London , 935 (1883).

[3] E. R. Meinders, *Experimental study of heat transfer in turbulent flows over wall-mounted cubes.* (1998).

[4] X. Yang and C. Meneveau, *Modelling turbulent boundary layer flow over fractal-like multiscale terrain using large-eddy simulations and analytical tools,* Philosophical Transactions of the Royal Society A: Mathematical, Physical and Engineering Sciences **375**, 20160098 (2017).

[5] H. Khanbareh, *Fractal dimension alaysis of grain boundaries of 7xxx aluminum alloys and its relationship to fracture toughness,* Delft University of Technology, nd (2011).

[6] J. Tomas, *Obstacle-resolving large-eddy simulation of dispersion in urban environments: Effects of stability and roughness geometry*, Ph.D. thesis, Delft University of Technology (2016).

[7] P. Forooghi, M. Stripf, and B. Frohnapfel, *A systematic study of turbulent heat transfer over rough walls,* International Journal of Heat and Mass Transfer **127**, 1157 (2018).

[8] M. Chyu and V. Natarajan, *Heat transfer on the base surface of threedimensional protruding elements,* International Journal of Heat and Mass Transfer **39**, 2925 (1996).

[9] S. B. Pope, *Turbulent flows,* (2001).

[10] F. T. Nieuwstadt, J. Westerweel, and B. J. Boersma, *Turbulence: introduction to theory and applications of turbulent flows* (Springer, 2016).

[11] J. Jiménez, *Turbulent flows over rough walls,* Annu. Rev. Fluid Mech. **36**, 173 (2004).

[12] X. Zhu, G. V. Iungo, S. Leonardi, and W. Anderson, *Parametric study of urban-like topographic statistical moments relevant to a priori modelling of bulk aerodynamic parameters,* Boundary-Layer Meteorology **162**, 231 (2017).

[13] K. A. Flack and M. P. Schultz, *Review of hydraulic roughness scales in the fully rough regime,* Journal of Fluids Engineering **132**, 041203 (2010).

[14] C. Grimmond and T. R. Oke, *Aerodynamic properties of urban areas derived from analysis of surface form,* Journal of applied meteorology **38**, 1262 (1999).

[15] H. Schlichting, *Experimental investigation of the problem of surface roughness,* (1937).

[16] J. Nikuradse, *Laws of flow in rough pipes naca technical memorandum (1292),* (1933).

[17] Y. Wu and K. Christensen, *Outer-layer similarity in the presence of a practical rough-wall topography,* Physics of Fluids **19**, 085108 (2007).

[18] J. A. Van Rij, B. Belnap, and P. Ligrani, *Analysis and experiments on three-dimensional, irregular surface roughness,* Journal of fluids engineering **124**, 671 (2002).

[19] C. Vanderwel and B. Ganapathisubramani, *Turbulent boundary layers over multiscale rough patches,* Boundary-Layer Meteorology **172**, 1 (2019).

[20] H. Cheng and I. P. Castro, *Near wall flow over urban-like roughness,* Boundary-Layer Meteorology **104**, 229 (2002).

[21] D. Aliaga, J. Lamb, and D. E. Klein, *Convection heat transfer distributions over plates with square ribs from infrared thermography measurements,* International journal of heat and mass transfer **37**, 363 (1994).

[22] P. Orlandi, D. Sassun, and S. Leonardi, *Dns of conjugate heat transfer in presence of rough surfaces,* International Journal of Heat and Mass Transfer **100**, 250 (2016).

[23] Y. Miyake, K. Tsujimoto, and M. Nakaji, *Direct numerical simulation of rough-wall heat transfer in a turbulent channel flow,* International Journal of Heat and Fluid Flow **22**, 237 (2001).

[24] A. M. Anderson, *Convective heat transfer from arrays of modules with non-uniform heating: experiments and models* (Stanford University, 1990).

[25] D. Wroblewski and P. Eibeck, *Turbulent heat transport in a boundary layer behind a junction of a streamlined cylinder and a wall,* Journal of heat transfer **114**, 840 (1992).

[26] O. Coceal, T. Thomas, I. Castro, and S. Belcher, *Mean flow and turbulence statistics over groups of urban-like cubical obstacles,* Boundary-Layer Meteorology **121**, 491 (2006).

[27] S. E. Belcher, *Mixing and transport in urban areas,* Philosophical Transactions of the Royal Society A: Mathematical, Physical and Engineering Sciences **363**, 2947 (2005).

[28] R. Macdonald, R. Griffiths, and D. Hall, *An improved method for the estimation of surface roughness of obstacle arrays,* Atmospheric environment **32**, 1857 (1998).

[29] B. B. Mandelbrot, *The fractal geometry of nature*, Vol. 173 (WH freeman New York, 1983).

[30] A. Majumdar and C. Tien, *Fractal network model for contact conductance,* Journal of Heat Transfer **113**, 516 (1991).

[31] Y. Chen, C. Zhang, M. Shi, and G. P. Peterson, *Optimal surface fractal dimension for heat and fluid flow in microchannels,* Applied Physics Letters **97**, 084101 (2010).

[32] W. Hundsdorfer, B. Koren, M. Van Loon, and J. Verwer, *A positive finite-difference advection scheme,* Journal of computational physics **117**, 35 (1995).

[33] S. Gottlieb and C.-W. Shu, *Total variation diminishing runge-kutta schemes,* Mathematics of computation **67**, 73 (1998).

[34] W. Breugem and B. Boersma, *Direct numerical simulations of turbulent flow over a permeable wall using a direct and a continuum approach,* Physics of fluids **17**, 025103 (2005).

[35] Y. Nagano, H. Hattori, and T. Houra, *Dns of velocity and thermal fields in turbulent channel flow with transverse-rib roughness,* International Journal of Heat and Fluid Flow **25**, 393 (2004).

[36] P. Forooghi, A. Weidenlener, F. Magagnato, B. Boehm, H. Kubach, T. Koch, and B. Frohnapfel, *Dns of momentum and heat transfer over rough surfaces based on realistic combustion chamber deposit geometries,* International Journal of Heat and Fluid Flow **69**, 83 (2018).

[37] M. MacDonald, N. Hutchins, and D. Chung, *Roughness effects in turbulent forced convection,* Journal of Fluid Mechanics **861**, 138 (2019).

[38] L. Ventola, F. Robotti, M. Dialameh, F. Calignano, D. Manfredi, E. Chiavazzo, and P. Asinari, *Rough surfaces with enhanced heat transfer for electronics cooling by direct metal laser sintering,* International Journal of Heat and Mass Transfer **75**, 58 (2014).

[39] H. Lu, M. Xu, L. Gong, X. Duan, and J. C. Chai, *Effects of surface roughness in microchannel with passive heat transfer enhancement structures,* International Journal of Heat and Mass Transfer **148**, 119070 (2020).

[40] M. Placidi and B. Ganapathisubramani, *Turbulent flow over large roughness elements: effect of frontal and plan solidity on turbulence statistics and structure,* Boundary-layer meteorology **167**, 99 (2018).

[41] S. Leonardi, P. Orlandi, and R. A. Antonia, *Heat transfer in a turbulent channel flow with roughness,* in *Fifth International Symposium on Turbulence and Shear Flow Phenomena* (Begel House Inc., 2007).

[42] A. F. Mills, *Basic heat and mass transfer* (Prentice hall, 1999).

[43] R. J. Phillips, *Forced-convection, liquid-cooled, microchannel heat sinks*, Ph.D. thesis, Massachusetts Institute of Technology (1987).

[44] W. M. Kays, *Convective heat and mass transfer* (Tata McGraw-Hill Education, 2012).

[45] T. L. Bergman, F. P. Incropera, D. P. DeWitt, and A. S. Lavine, *Fundamentals of heat and mass transfer* (John Wiley & Sons, 2011).